The Effect of Flow and Mixture Inhomogeneity on the Dynamics of Strained Flames

by

Youssef Mohamed Marzouk

S.B., Massachusetts Institute of Technology (1997)

Submitted to the Department of Mechanical Engineering
in partial fulfillment of the requirements for the degree of

Master of Science in Mechanical Engineering

at the

MASSACHUSETTS INSTITUTE OF TECHNOLOGY

August 1999

Author .....
Department of Mechanical Engineering
August 23, 1999

Certified by .....
Ahmed F. Ghoniem
Professor of Mechanical Engineering
Thesis Supervisor

Accepted by .....
Ain A. Sonin
Chairman, Department Committee on Graduate Students

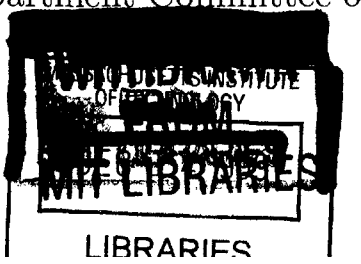

The Effect of Flow and Mixture Inhomogeneity on the Dynamics of Strained Flames

by

Youssef Mohamed Marzouk

Submitted to the Department of Mechanical Engineering
on August 23, 1999, in partial fulfillment of the
requirements for the degree of
Master of Science in Mechanical Engineering

Abstract

Changes in flow strain and mixture composition on the order of a flame time scale are characteristic of many practical combustion processes. Accurately predicting the unsteady reponse of burning to these changes requires detailed modeling of species transport and chemical kinetics. This thesis formulates a detailed one-dimensional computational model for arbitrary unsteady conditions of strain and mixture, demonstrating its applicability to subgrid modeling of turbulent combustion. A novel numerical formulation, based on a globalized Newton iterative method and a preconditioned Krylov subspace linear solver, ensures efficient and robust convergence despite the stiffness of detailed chemistry. The model is validated via comparison with OPPDIF, a well-benchmarked steady-state strained flame code. The model is then used to characterize the fundamental interactions of flow and mixture inhomogeneity—examining the dynamic response of flame structure and burning to linear variations in mixture equivalence ratio, and capturing the effect of unsteady strain on a flame surface interacting with a vortex in two dimensions. The latter example leads to a redefinition of the appropriate subgrid strain for flame embedding simulation of premixed turbulent combustion.

Thesis Supervisor: Ahmed F. Ghoniem
Title: Professor of Mechanical Engineering

Acknowledgments

Thanks are first due to my thesis advisor, Professor Ahmed Ghoniem. His guidance and insight have brought coherence and rigorous thinking to this work, as well as a strong awareness of its context and implications. I would also like to thank Dr. Habib Najm, who hosted me at Sandia National Laboratories in August of 1998, during the early stages of this effort. His attention to detail and his practical know-how, shared in many discussions over the past year, helped speed the progress of my research. Also, Habib generously provided the data from simulations of flame-vortex interaction that are used in this thesis.

I owe a debt of gratitude to my family, who have been constant and supportive throughout my education; my appreciation of their support continues to grow. Thanks are also due to my fellow students (and postdocs) at the Reacting Gas Dynamics Lab—Jean-Pierre Hathout, Issam Lakkis, Shankar Subramaniam, and Mahmoud Fleifil. I have relied on them for friendship, technical advice, and a healthy share of lunchtime diversion. I also thank Constantin Petrov, a laboratory alumnus, for introducing me to the elemental flame code.

Finally, I would like to acknowledge the support of the Fannie and John Hertz Foundation, which has sponsored me as a graduate fellow for the past two years. Numerical simulations in this thesis were performed at Sandia National Laboratories, through a collaboration supported by the United States Department of Energy.

Contents

List of Figures

List of Tables

Chapter 1

Introduction

Combustion is a dynamically complex process, reliant on the interplay of fluid flow, diffusive transport, and chemical kinetics, all occurring over a wide range of length and time scales. Computational simulation of combustion in practical devices necessarily applies simplifying assumptions to these physical processes. Indeed, full numerical simulation of multi-dimensional reacting flow—simulation that resolves all spatial and temporal scales of turbulence and chemistry—is far beyond the reach of current computer technology, and will not be feasible in the forseeable future.

A classical practice in combustion simulation has been to assume instantaneous response of the flame to dynamic changes in flow or mixture composition, using such devices as a flamelet library or some other closure scheme based on steady-state flame properties. Yet there is a whole range of combustion processes for which this assumption is not valid; combustion instability, combustion at high turbulence intensity, and combustion in stratified charges are but a few phenomena in which flow and mixture composition changes on the order of a flame time scale do occur. Capturing the dynamic, *unsteady* response of flames is thus essential to a physical understanding of these phenomena. Modeling the effect of such flow and mixture inhomogeneities is the focus of work in this thesis.

1.1 Turbulent Combustion Simulation

Combustion in a turbulent flow may take the form of a flame surface convoluted over a range of length scales by vortical structures. The area and burning rate of this flame surface is primarily affected by the hydrodynamic strain, i.e., the continually varying strain rate imposed by turbulent eddies. Figures 1-1 and 1-2 demonstrate the interaction of turbulence with a two-dimensional flame front. Figure 1-1 shows snapshots of a premixed flame interacting with a vortex at 0.5 ms intervals, extracted from a direct numerical simulation; Figure 1-2 shows a flame front in a sea of homogeneous turbulence, also obtained via direct numerical simulation. In both cases, the flame is a thin surface wrapped around vortical structures, and the evolutions of the flame surface and the flow structures are dynamically linked.

Of course, this model is not applicable to all regimes of turbulent combustion. Turbulent combustion processes may be classified by Damköhler and Karlovitz numbers, as seen in Figure 1-3. The Damköhler number is the ratio of the flow (integral) time scale to chemical time scale

$$Da = \frac{\tau_F}{\tau_R} \tag{1.1}$$

while the Karlovitz number is taken as the ratio of the flame stretch rate to a critical stretch rate, using l_F as a flame thickness and s_L as the laminar flame speed:

$$Ka = \frac{\frac{1}{A}\frac{dA}{dt}}{s_L/l_F} \tag{1.2}$$

The limit of fast chemistry corresponds to $Da \gg 1$, while one expects local quenching and distributed reaction zones for $Ka > 1$. Thus the model of a continuous flame surface wrinkled or corrugated by turbulence, as described above, is valid in the regime $Da \gg 1$, $Ka \leq 1$.

In this "flamelet" regime of turbulent combustion, the flame surface occupies only a fraction of the total volume of reacting flow. Yet solving the fully coupled equations of reacting flow with detailed chemistry, as in Figures 1-1 and 1-2 is computationally very expensive, prohibitive for all but the most idealized cases. It would be

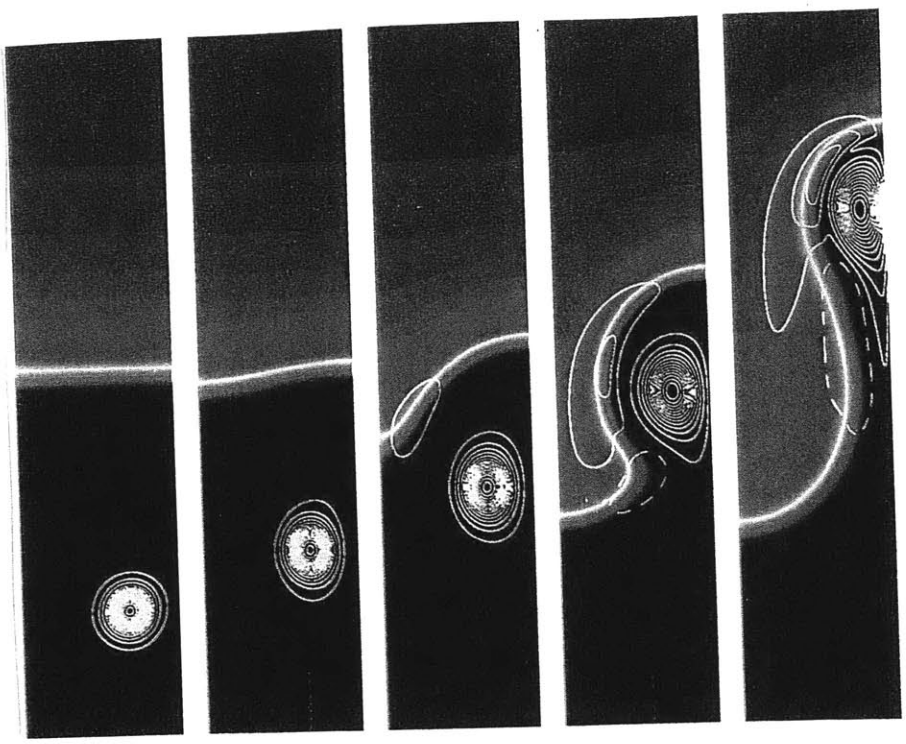

Figure 1-1: Full numerical simulation of flame-vortex interaction.

desirable—for the purposes of computational efficiency, and as a fundamental modeling advance—to decouple the flame surface from the non-reacting portions of the flow, to develop a *subgrid model* for the flame, specifically, one that captures the unsteady effects of strain imposed by the flow. Modeling a turbulent reacting flow in the flamelet regime would thus consist of dynamically coupling a non-reacting flow solver with this subgrid model, the flow straining the flame and changing its burning rate, the flame acting as a source of volumetric expansion and a baroclinic source of vorticity in the flow. This idea is known as flame embedding, and has been explored in its initial stages [22]. A detailed and accurate subgrid model is central to the success of the flame embedding technique and will be developed in subsequent chapters.

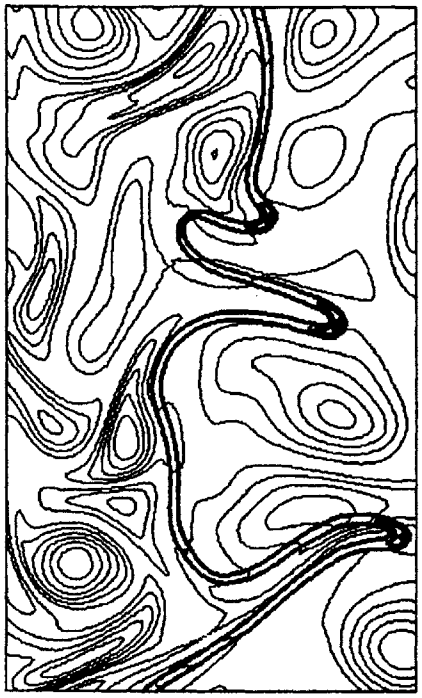

Figure 1-2: Flame surface in homogeneous turbulence.

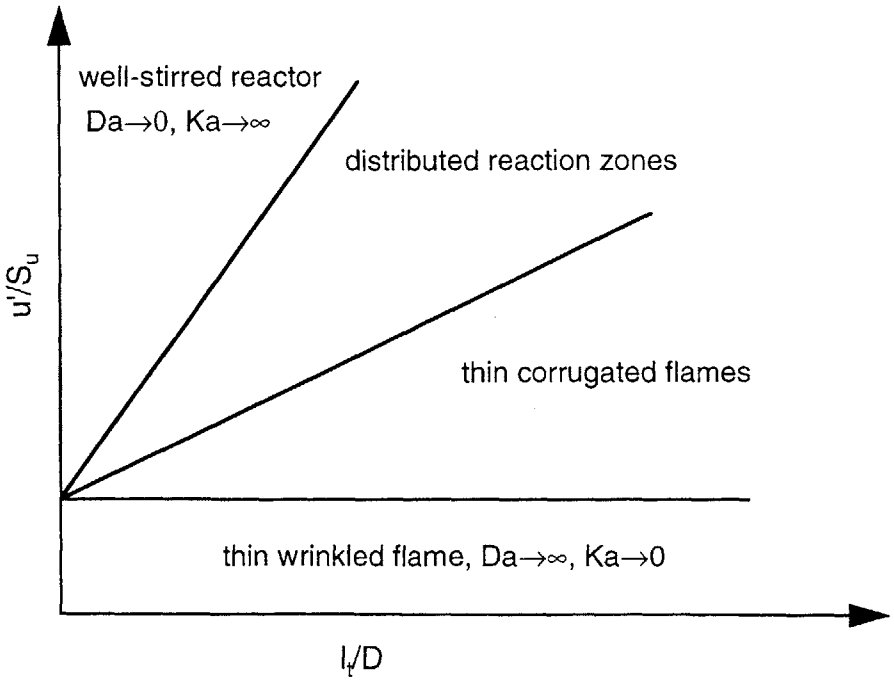

Figure 1-3: Phase diagram of turbulent combustion.

1.2 Flame Response to Unsteady Strain

Many studies have examined the response of premixed or non-premixed laminar flames to unsteady strain rates, most often for the purposes of understanding the effect of turbulence on burning [34, 12, 23, 25, 3, 9, 26, 24, 11, 13, 5]. Strain affects a flame by changing scalar gradients and thus the rates of diffusive transport feeding the flame. Accurately predicting the effects of strain therefore requires detailed models for chemistry and species transport. However, certain qualitative results can be summarized:

Consider a premixed flame in which, for simplicity, a single Lewis number ($Le \equiv \alpha/D$) describes the transport of all species. The direct impact of strain is on the convection-diffusion zone of the flame, but the actual effect of strain on burning, i.e., on the reaction zone, depends closely on the Lewis number. For a unity Lewis number, mass and heat diffusion rates are equal, and the reaction-diffusion zone is essentially unaffected over a range of weak to intermediate strains. Once the flow time scale imposed by the strain becomes comparable to the chemical time scale, however, the temperature in the reaction zone begins to fall and the burning rate decreases. Here the Karlovitz number is of order unity; at even higher strains (and values of Ka), flame extinction may be observed.

For nonunity Lewis number, the imbalance between mass and heat flux leads to changes in flame structure at weak and intermediate strains. Strain shifts values of temperature and fuel mass fraction relative to one another, thus altering the conditions in the reaction zone. For $Le > 1$, heat diffuses more quickly than mass; a smoother temperature profile reduces the temperature in the reaction zone, and the burning rate decreases monotonically with strain. For $Le < 1$, fuel diffuses more quickly than heat, and temperature actually increases at the location of the maximum reaction rate; the burning rate thus increases with weak to intermediate strain.

At high strain, Lewis number effects become less important. As described above for unity Lewis number, the burning rate at $Ka > 1$ must decrease for nonunity and unity Lewis number flames alike. Flame extinction occurs as the influx of cold

reactants exceeds the rate of heat release from chemical reaction and the reaction zone falls below the ignition temperature. Numerical results supporting these trends can be found in [23].

Of course, a single Lewis number applied to all species cannot describe a real reacting flow. This simplified discussion of strain at varying Lewis numbers emphasizes the importance of detailed chemistry and transport in accurately modeling a flame, even to predict the steady-state effect of a given strain rate. In a realistic flame, the diffusive flux of each mixture component reacts differently to a change in strain rate, and the superposition of these diffusive fluxes changes the composition and temperature of the reaction zone, where, in turn, a complex set of chemical pathways determines the burning rate.

Now consider unsteady strain rates: The effect of oscillatory strain on a flame depends on the frequency of the applied oscillations. At low frequency the flame may respond in a quasi-steady manner; at moderate frequency, the flame responds with a time lag, and thus a phase shift; while at even higher frequency, a flame may be unresponsive to oscillations in strain. The bounds between these regimes depend on the relative sizes of the flame time scale and the period of strain oscillations. It is also important to note that a flame may survive at higher unsteady strains than it would in a steady-state environment, a result reported by Najm [16] and others. Moreover, flames in a turbulent environment can undergo quenching and subsequent re-ignition. All these effects must be captured to model the effects of flow inhomogeneity on combustion.

1.3 Flame Response to Unsteady Mixture

The response of flames to unsteady changes in mixture composition, or more specifically, to unsteady changes in equivalence ratio, has not been studied extensively. However, spatial or temporal stratification of a reacting mixture occurs in numerous practical devices. An outstanding example of this—with unsteadiness on the order of a flame time scale—occurs in combustion instability and its control.

Consider the combustor shown schematically in Figure 1-4. Perturbations in the heat release rate of the flame will lead to pressure perturbations in the combustion chamber. If the fuel flow is choked or constant, as with a fuel injector, pressure perturbations will affect only the air flow and thus create variation in the equivalence ratio of the mixture reaching the flame. This perturbation in ϕ then affects the heat release in the flame, and a positive feedback can occur, leading to instability. Equivalence-ratio driven combustion instabilities like this have been observed in practice, and discussed in the literature [29].

The preceding argument may be cast in a more rigorous, mathematical form. The heat release rate $\dot{q}$ acts as a source term in the standard wave equation:

$$\frac{\partial^2 p'}{\partial t^2} - c^2 \frac{\partial^2 p'}{\partial x^2} = (\gamma - 1)\,\dot{q} \tag{1.3}$$

Now using a Galerkin expansion and focusing on only one acoustic mode, we obtain an oscillator equation.

$$p' = \eta(t)\psi(x) \longrightarrow \ddot{\eta}' + \omega^2 \eta = c\dot{q} \tag{1.4}$$

The heat release rate $\dot{q}$ depends on both the velocity and equivalence ratio perturbations, and the equivalence ratio perturbation is some function of p' and $\dot{p}'$. The first of these relationships must incorporate the character of unsteady flame response. Under appropriate conditions, the functional form of $\dot{q}$ will introduce a negative term in $\dot{p}'$ on the left-hand side of the oscillator equation; this negative damping is indicative of combustion instability.

Combustion instability is typically observed at frequencies of 100–1000 Hz, implying mixture inhomogeneity on the order of a flame time scale. Moreover, even when combustion instability is not driven by equivalence ratio, control actuation mechanisms such as fuel injection can still introduce equivalence ratio variation at similar frequencies.

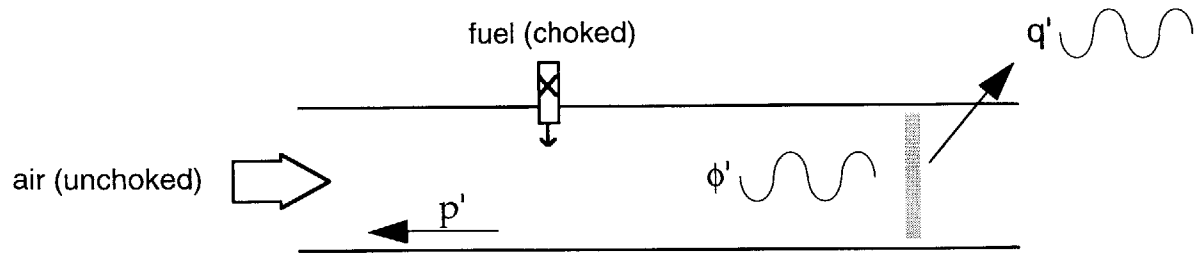

Figure 1-4: Schematic of equivalence-ratio driven combustion instability.

1.4 Scope and Goals

Motivated by the physical problems presented above, this thesis will develop a simple computational model applicable to flame embedding and to arbitrary unsteady conditions of strain and mixture. The formulation of this model is presented in Chapter 2.

To accurately predict unsteady flame response, our model must incorporate detailed chemical kinetics and species transport. Many detailed-chemistry flame codes are currently available, but most of these codes are aimed at steady-state problems. Also, these codes tend to lack numerical robustness and to exhibit poor efficiency. Thus an important thrust of this work will be to develop more robust, computationally efficient numerical methods for stiff, multi-species reacting flow. Implementation of these numerical methods is described in Chapter 3.

The remainder of the thesis will focus on applications of the computational model. Validation of the model, through direct comparison with a well-benchmarked steady-state flame code (Sandia's OPPDIF) is presented in Chapter 4. Chapter 5 finally uses the code to examine several unsteady problems discussed in the preceding sections: first, the burning of a stratified mixture, and second, a comparison with direct numerical simulation of two-dimensional turbulent combustion, thereby refining the concepts of flame embedding.

Chapter 2

Model Formulation

Turbulent combustion in the "flamelet" regime, as described in §1.1, takes the form of a thin flame surface strained by turbulent eddies. Our goal is to develop a model that captures the effect of flow strain and changing mixture composition on this surface—in other words, an unsteady subgrid model applicable to flame embedding. Though motivated by a physical picture of turbulent flow, this model also will lend itself to more idealized studies of arbitrary strain and mixture inhomogeneity.

2.1 Kinematics of Flame Front Stretching

The first assumption of our model is suggested by the thinness of a turbulent flame surface in the flamelet regime. Fast chemistry ($Da \gg 1$) and a high rate of heat release insure that scalar gradients normal to the flame surface are much larger than those tangential to it. Neglecting the tangential gradients, one obtains a locally one-dimensional flame structure.

Now consider the kinematics of a material element on a two-dimensional flame front, as shown in Figure 2-1. The motion of any such fluid line segment may be decomposed into translation, rotation, and strain. In flame coordinates—that is, in the reference frame of the fluid line segment—the only effect of motion that will be apparent is that of strain. Translation and rotation may change the mixture that the flame front encounters, but only strain will alter the flame's internal structure. The

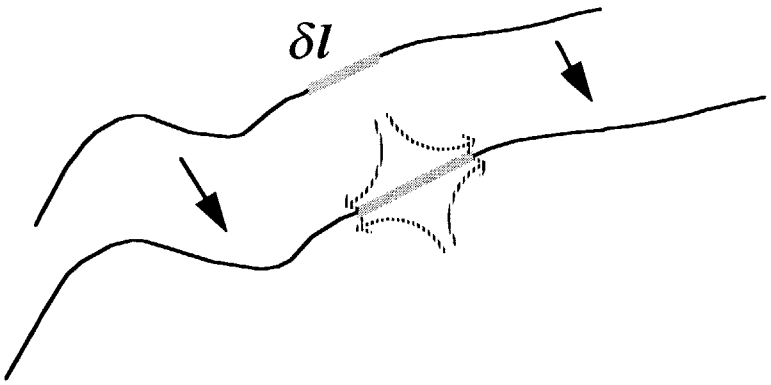

Figure 2-1: Deformation of material element on a flame front.

strain is given by the relative change in length of the line segment:

$$\epsilon = \frac{1}{|\delta \mathbf{l}|}\frac{d\delta \mathbf{l}}{dt} = \frac{\delta \mathbf{l} \cdot \nabla \mathbf{u}}{|\delta \mathbf{l}|} \tag{2.1}$$

Further insight may be obtained by decomposing the flow local to the flame front. Figure 2-2 shows two initially perpendicular line segments, l and m, in a reference frame $\mathcal{F}$ chosen to follow a flame element. The x-axis of this reference frame is always parallel to the flame surface, while the y-axis is always perpendicular to it. The line segment l is a material element of the flame front and thus always lies on the x-axis, while the line segment m is initially coincident with the y-axis. At an initial time t, the projections of the the line segments on the axes are

$$l_x(t) = l(t),\ l_y(t) = 0 \tag{2.2}$$

$$m_x(t) = 0,\ m_y(t) = m(t) \tag{2.3}$$

After an elapsed time dt, the projections become

$$l_x(t+dt) = \left(1 + \frac{\partial u}{\partial x}dt\right) l(t) \tag{2.4}$$

$$l_y(t+dt) = \left(\frac{\partial v}{\partial x}dt\right) l(t) = 0 \tag{2.5}$$

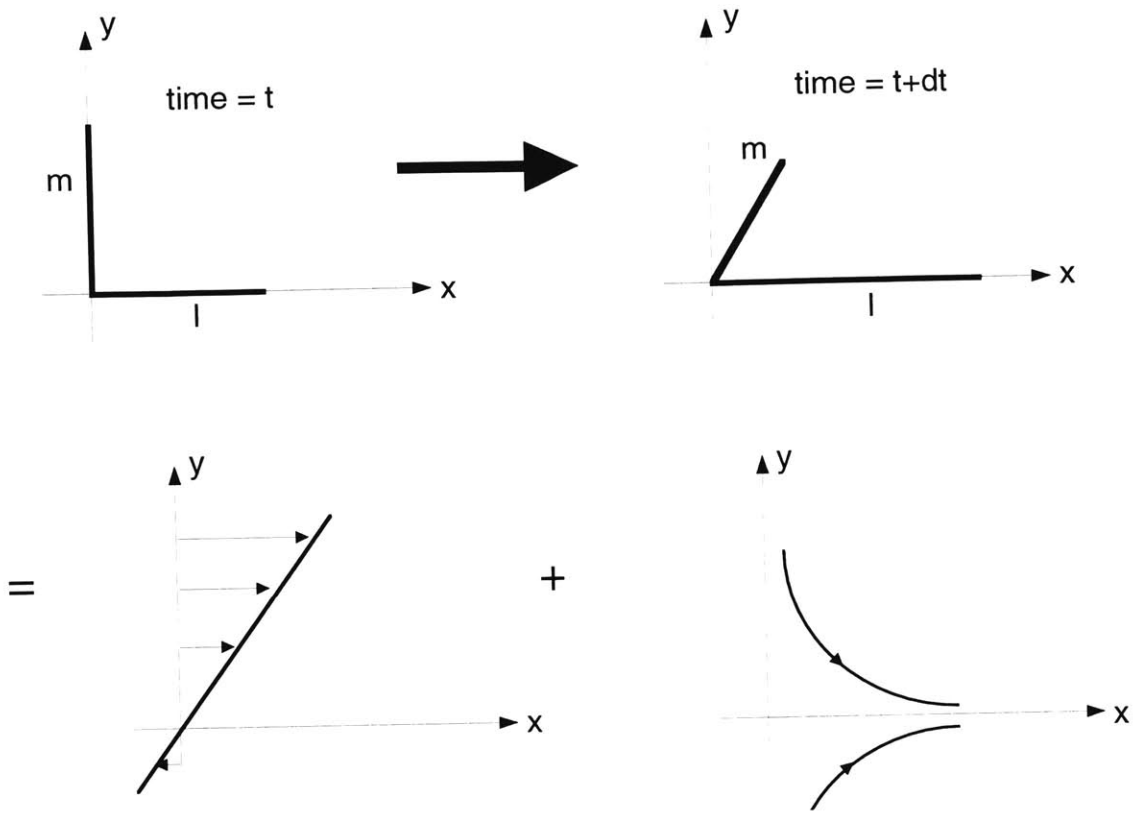

Figure 2-2: Flow-induced deformation in the reference frame of a flame element.

$$m_x(t+dt) = \left(\frac{\partial u}{\partial y}dt\right) m(t) \tag{2.6}$$

$$m_y(t+dt) = \left(1 + \frac{\partial v}{\partial y}dt\right) m(t) \tag{2.7}$$

where u and v are the flow velocities in the x and y directions, respectively. Note that our choice of reference frame requires the derivative in Equation 2.5 to equal zero.

As expressed in Equation 2.6, the projection m_x grows at the rate $\partial u/\partial y$; the segment initially in the y-direction thus rotates without changing its length. This deformation is consistent with a *pure shear flow*, corresponding to off-diagonal components of the strain rate tensor:

$$\tau_{xy} = \frac{1}{2}\left(\frac{\partial u}{\partial y} + \frac{\partial v}{\partial x}\right) \tag{2.8}$$

The second component of flow local to the flame element is a *stagnation point flow*,

observed in Equations 2.4 and 2.7. Both line segments are strained along the principal axes, and because of continuity in an incompressible flow, the rates of strain are equal and opposite in sign:

$$\epsilon = \frac{\partial u}{\partial x} = -\frac{\partial v}{\partial y} \tag{2.9}$$

Decomposition of the flow in the vicinity of a flame element is shown schematically in Figure 2-2.

What does this flow decomposition imply for modeling the effect of inhomogeneities on a flame surface? As stated earlier, scalar gradients (e.g., gradients of temperature, density, species concentrations) normal to the flame are much larger than those tangential to the flame. In the reference frame $\mathcal{F}$, this can be written

$$\frac{\partial}{\partial x} \ll \frac{\partial}{\partial y} \tag{2.10}$$

Now consider the transport equation for a scalar in $\mathcal{F}$; this equation must contain the following differential operator:

$$\mathcal{L} \equiv \frac{\partial}{\partial t} + u\frac{\partial}{\partial x} + v\frac{\partial}{\partial y} - \frac{\partial^2}{\partial x^2} - \frac{\partial^2}{\partial y^2} \tag{2.11}$$

The velocity of the shear flow, $u_{shear} = cy$, contributes only to the u in the second term of Equation 2.11. Following Equation 2.10, this second term can be neglected entirely, rendering the shear component of the velocity field unimportant in local transport of scalars. Physically, this can be understood from Figure 2-2; the shear field simply advects constant values of scalars parallel to the flame surface and cannot alter the distribution of scalars normal to the flame. As a result, the instantaneous burning of a turbulent flame surface is locally similar to that of a stagnation point flow with an appropriately chosen strain rate. Our subgrid model for the effect of strain and mixture inhomogeneity on burning will center on this stagnation point flow.

It is important to note that the preceding analysis does not account for curvature of the flame surface. (The line segments displaced in Figures 2-1 and 2-2 are perfectly

straight.) Propagation of a curved flame contributes to the total stretch rate as follows:

$$\frac{1}{|\delta \mathbf{l}|}\frac{d\delta \mathbf{l}}{dt} = \epsilon + 2s_d h_m \tag{2.12}$$

where ϵ is the ordinary hydrodynamic strain, given by the surface divergence of the velocity field, s_d is the speed of the flame surface normal to itself, and h_m is the mean curvature. This effect is relevant only to premixed flames ($s_d \neq 0$), and typically becomes important only in regions of high curvature (where the radius of curvature is small relative to the flame thickness)—in the cusp of a vortical structure, for example. For simplicity, the flame models used in this thesis will ignore curvature effects.

Finally, it is instructive to contrast our subgrid model with traditional flamelet models for turbulent combustion, as developed by Bray [2]. Both models represent local burning conditions of the flame surface with a stagnation point flow, but the model developed here will has the distinction of being *unsteady*. As discussed in Chapter 1, the effects of unsteadiness are fundamental to the dynamics of flame-flow interaction, and modeling them takes an important step towards accurate simulation of reacting flow.

2.2 Governing Equations for the Elemental Flame

The unsteady combustion zone model developed in this chapter is known as the *elemental flame* model, distinguishing it from the quasi-steady flamelet approach [22]. Consider a flame strained in a planar stagnation point flow, with coordinates and flow velocities shown in Figure 2-3. The flame introduces directionality to this figure and enables use of the boundary layer approximation; for any scalar φ, gradients parallel to the flame $\partial^2\varphi/\partial x^2$ are negligible compared to those perpendicular to the flame, $\partial^2\varphi/\partial y^2$. We thus write unsteady boundary layer equations for transport of species, energy, momentum, and mass:

$$\rho\frac{\partial Y_k}{\partial t} + \rho u\frac{\partial Y_k}{\partial x} + \rho v\frac{\partial Y_k}{\partial y} = \frac{\partial}{\partial y}\left(\rho D_k\frac{\partial Y_k}{\partial y}\right) + \dot{w}_k W_k \tag{2.13}$$

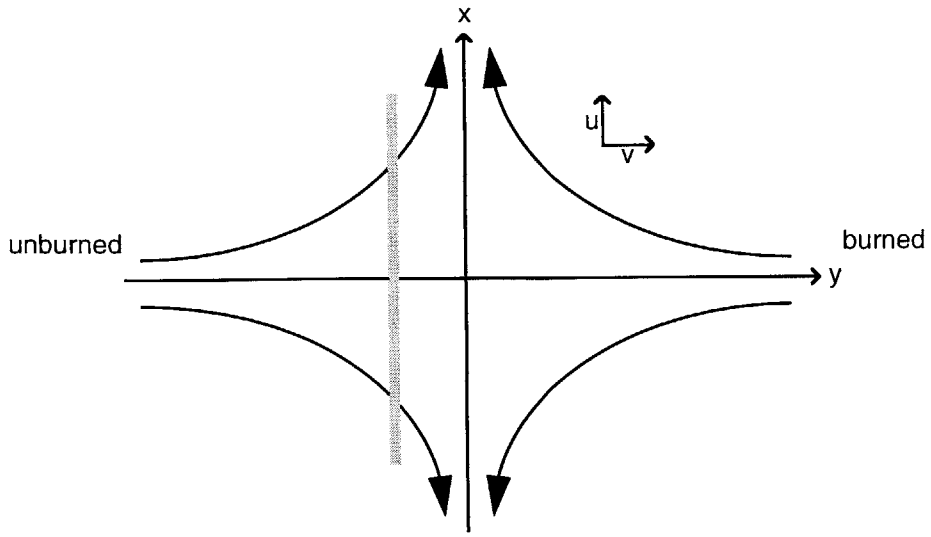

Figure 2-3: Flame strained in a stagnation point flow; the elemental flame model.

$$\rho\frac{\partial T}{\partial t}+\rho u\frac{\partial T}{\partial x}+\rho v\frac{\partial T}{\partial y}=\frac{1}{C_p}\frac{\partial}{\partial y}\left(\lambda\frac{\partial T}{\partial y}\right)+\sum_k\frac{\dot{w}_k h_k}{C_p} \tag{2.14}$$

$$\rho\frac{\partial u}{\partial t}+\rho u\frac{\partial u}{\partial x}+\rho v\frac{\partial u}{\partial y}=-\frac{\partial p}{\partial x}+\frac{\partial}{\partial y}\left(\mu\frac{\partial u}{\partial y}\right) \tag{2.15}$$

$$\frac{\partial \rho}{\partial t}+\frac{\partial(\rho u)}{\partial x}+\frac{\partial(\rho v)}{\partial y}=0 \tag{2.16}$$

Here Y_k is the mass fraction of species k, D_k is the mixture-averaged diffusion coefficient for species k, while W_k and $\dot{w}_k$ are the molecular weight and molar production rate for species k, respectively. In the remaining equations, C_p is the mixture-averaged specific heat, λ is the thermal conductivity, h_k is the molar specific heat of species k, p is the hydrodynamic pressure, and μ is the absolute viscosity of the mixture. Note that the enthalpy flux term is neglected in the energy equation (Equation 2.14) while thermal diffusion velocity is neglected in each species transport equation (Equation 2.13). Smooke [33] and others have shown that both effects are unimportant to the laminar strained flame.

The pressure gradient dp/dx inside the boundary layer is identical to that in the outer stagnation point flow, since by the usual boundary layer assumption, Δp across the boundary layer is negligible. Substituting the stagnation point flow velocity

profile $u_\infty = \epsilon(t)\, x,\ v_\infty = -\epsilon(t)\, y$ into the general x-direction momentum conservation equation, we obtain the pressure gradient as a function of the imposed strain:

$$\frac{\partial p}{\partial x} = -\rho_{ub} u_\infty \epsilon - \rho_{ub} \frac{u_\infty}{\epsilon} \frac{\partial \epsilon}{\partial t} \tag{2.17}$$

The notation ρ_{ub} above emphasizes that the density of the *unburned* mixture is used to define the pressure gradient. In the diffusion flame, densities outside of the boundary layer are equal, $\rho_{ub} = \rho_{-\infty} = \rho_\infty$, so this distinction is moot. In the premixed flame, however, heat release within the flame leads to a products-side stream entering with lower density—and to maintain a constant pressure gradient, a higher effective strain. Defining the global strain ϵ on the unburned side, in accordance with the expression for pressure gradient above, thus insures consistency and clarity across all flame configurations.

Introducing the notation $U \equiv u/u_\infty,\ V \equiv \rho v$, and substituting the pressure gradient expression into the equation for momentum conservation inside the boundary layer (Equation 2.15), Equations 2.13–2.16 can be rewritten as follows:

$$\rho \frac{\partial Y_k}{\partial t} + \rho u_\infty U \frac{\partial Y_k}{\partial x} + V \frac{\partial Y_k}{\partial y} = \frac{\partial}{\partial y}\left(\rho D_k \frac{\partial Y_k}{\partial y}\right) + \dot{w}_k W_k \tag{2.18}$$

$$\rho \frac{\partial T}{\partial t} + \rho u_\infty U \frac{\partial T}{\partial x} + V \frac{\partial T}{\partial y} = \frac{1}{C_p} \frac{\partial}{\partial y}\left(\lambda \frac{\partial T}{\partial y}\right) + \sum_k \frac{\dot{w}_k h_k}{C_p} \tag{2.19}$$

$$\rho u_\infty \frac{\partial U}{\partial t} + \rho u_\infty U \frac{1}{\epsilon} \frac{\partial \epsilon}{\partial t} + \rho u_\infty^2 U \frac{\partial U}{\partial x} + \rho u_\infty U^2 \epsilon + u_\infty V \frac{\partial U}{\partial y} = \rho_{ub} u_\infty \left(\frac{1}{\epsilon} \frac{\partial \epsilon}{\partial t} + \epsilon\right) + u_\infty \frac{\partial}{\partial y}\left(\mu \frac{\partial U}{\partial y}\right) \tag{2.20}$$

$$\frac{\partial \rho}{\partial t} + u_\infty U \frac{\partial \rho}{\partial x} + \rho U \epsilon + \rho u_\infty \frac{\partial U}{\partial x} + \frac{\partial V}{\partial y} = 0 \tag{2.21}$$

Now consider the solution of the boundary layer equations along the stagnation streamline, $x = 0$. Along this streamline, $u = u_\infty U = 0$ and by symmetry, $\partial\varphi/\partial x = 0$, where φ is a passive scalar—namely, T, Y_k, U, or ρ. Thus, we can eliminate

the x-direction convective terms in Equations 2.18–2.21. Note, however, that $\partial u/\partial x$ and $\partial u_\infty/\partial x$ are nonzero on the stagnation streamline, and that this flow divergence should be reflected in the momentum and continuity equations. Every term in the momentum conservation equation (Equation 2.20) is proportional to u_∞, so to retain this equation in the system, we divide by u_∞. The resulting equation governs the strain rate through the reaction zone, where ϵU can be thought of as the effective strain. The final set of governing equations takes the following form:

$$\rho\frac{\partial Y_k}{\partial t} + V\frac{\partial Y_k}{\partial y} - \frac{\partial}{\partial y}\left(\rho D_k\frac{\partial Y_k}{\partial y}\right) - \dot{w}_k W_k = 0 \tag{2.22}$$

$$\rho\frac{\partial T}{\partial t} + V\frac{\partial T}{\partial y} - \frac{1}{C_p}\frac{\partial}{\partial y}\left(\lambda\frac{\partial T}{\partial y}\right) - \sum_k \frac{\dot{w}_k h_k}{C_p} = 0 \tag{2.23}$$

$$\rho\frac{\partial U}{\partial t} + \rho U\frac{1}{\epsilon}\frac{\partial \epsilon}{\partial t} + \rho U^2\epsilon + V\frac{\partial U}{\partial y} - \frac{\partial}{\partial y}\left(\mu\frac{\partial U}{\partial y}\right) - \rho_{ub}\left(\frac{1}{\epsilon}\frac{\partial \epsilon}{\partial t} + \epsilon\right) = 0 \tag{2.24}$$

$$\frac{\partial \rho}{\partial t} + \frac{\partial V}{\partial y} + \rho U\epsilon = 0 \tag{2.25}$$

Note that the low Mach number assumption has been used in the governing equations above. Density is calculated as a function of the temperature, species mass fractions, and thermodynamic pressure (assumed constant) via the ideal gas equation of state.

At various times, it will be useful to consider a flame strained in an axisymmetric stagnation point flow rather than in the planar configuration used above. Denoting the radial coordinate with r and the axial coordinate with y, the velocity profile of an axisymmetric stagnation point flow is $u_\infty = \epsilon(t)\, r$, $v_\infty = -2\epsilon(t)\, y$. The governing equations for this configuration are identical to those derived above (Equations 2.22–2.24) with the exception of the continuity equation. The revised continuity equation is:

$$\frac{\partial \rho}{\partial t} + \frac{\partial V}{\partial y} + 2\rho U\epsilon = 0 \tag{2.26}$$

Boundary conditions for the species and energy equations consist of defining the composition and temperature of the two incoming streams of the stagnation point

flow.

$$\begin{aligned} y = -\infty: \quad & Y_k = Y_{k,-\infty}, \quad T = T_{-\infty} \\ y = +\infty: \quad & Y_k = Y_{k,+\infty}, \quad T = T_{+\infty} \end{aligned} \tag{2.27}$$

The continuity equation requires only one boundary condition, which specifies zero velocity at the stagnation point:

$$y = 0: \quad V = 0 \tag{2.28}$$

The momentum conservation equation requires two boundary conditions. At an unburned stream, $u = u_\infty$, so the boundary condition is by definition $U = 1$. Setting the spatial gradients in Equation 2.24 to zero gives the boundary condition burned stream. This far-field boundary condition places an important requirement on the size of the computational domain; the flame must be far enough from the $+\infty$ and $-\infty$ boundaries for spatial gradients in U to vanish. In the case of steady strain, the burned-stream boundary condition on U is

$$U_b = \sqrt{\frac{\rho_{ub}}{\rho_b}} \tag{2.29}$$

where ρ_b is the density of the burned mixture. For unsteady strain, we must integrate the resulting ODE for U_b:

$$\frac{\partial U_b}{\partial t} = -U_b^2 \epsilon - U_b \left(\frac{1}{\epsilon} \frac{\partial \epsilon}{\partial t} \right) + \frac{\rho_{ub}}{\rho_b} \left(\frac{1}{\epsilon} \frac{\partial \epsilon}{\partial t} + \epsilon \right) \tag{2.30}$$

For a premixed flame, the effective strain rate in the incoming products-side mixture thus responds dynamically to the imposed strain rate.

2.3 Transport and Kinetics

To solve the system of governing equations derived in the preceding sections, every term must be expressed in terms of the fundamental variables: temperature, pressure, flow velocities, and mixture composition. Conductivity, viscosity, and species diffusion coefficients vary across the flame according to a prescribed transport model. The chemical source terms $\dot{w}_k$—molar production rates for each species—are complex functions of the local mixture conditions and thus depend on some chosen scheme of chemical kinetics, whether it is global or detailed. The models used to evaluate these terms are discussed below.

2.3.1 Transport Model

The transport coefficients μ, λ, and D_k could be evaluated exactly using Sandia's TRANSPORT package, an extension to CHEMKIN based on polynomial fits to empirical data. This approach is slow and cumbersome, however; instead we use the approximations validated by Smooke [33].

Smooke showed that the Lewis number of any given species does not vary significantly across the profile of a strained laminar flame. A fixed Lewis number $Le_k \equiv \alpha/D_k$ is thus chosen for each species, capturing the effects of multicomponent differential diffusion. The Prandtl number is chosen constant and equal to 0.75, while a curve fit is used to calculate the ratio λ/C_p in cgs units:

$$\frac{\lambda}{C_p} = 2.58 \times 10^{-4} \left(\frac{T}{298}\right)^{0.7} \tag{2.31}$$

This curve fit provides excellent results over a wide range of temperatures and pressures. The thermodynamic properties C_p and h_k are evaluated by CHEMKIN subroutines, polynomial functions of local mixture conditions.

For reference, the governing equations are restated below to incorporate the transport approximations just developed. Subsequent chapters will solve the equations in

this form.

$$\rho\frac{\partial Y_k}{\partial t} + V\frac{\partial Y_k}{\partial y} - \frac{\partial}{\partial y}\left(\frac{1}{Le_k}\frac{\lambda}{C_p}\frac{\partial Y_k}{\partial y}\right) - \dot{w}_k W_k = 0 \tag{2.32}$$

$$\rho\frac{\partial T}{\partial t} + V\frac{\partial T}{\partial y} - \frac{1}{C_p}\frac{\partial}{\partial y}\left(\lambda\frac{\partial T}{\partial y}\right) - \sum_k \frac{\dot{w}_k h_k}{C_p} = 0 \tag{2.33}$$

$$\rho\frac{\partial U}{\partial t} + \rho U\frac{1}{\epsilon}\frac{\partial \epsilon}{\partial t} + \rho U^2\epsilon + V\frac{\partial U}{\partial y} - Pr\frac{\partial}{\partial y}\left(\frac{\lambda}{C_p}\frac{\partial U}{\partial y}\right) - \rho_{ub}\left(\frac{1}{\epsilon}\frac{\partial \epsilon}{\partial t} + \epsilon\right) = 0 \tag{2.34}$$

$$\frac{\partial \rho}{\partial t} + \frac{\partial V}{\partial y} + \rho U\epsilon = 0 \tag{2.35}$$

2.3.2 Chemical Mechanism

The kinetic pathways of a combustion process typically consist of hundreds of elementary reactions among major and minor species, each with its own rate expression. These reactions together constitute a chemical mechanism, and can be simplified, or reduced, to an arbitrary level of detail. For example, if the steady-state heat release rate of a flame is the only variable of interest, a global mechanism with a single Arrhenius rate expression is sufficient. For detailed flame structure and for proper modeling of unsteady effects, however, a detailed kinetics mechanism is necessary (along with multicomponent transport), as discussed in Chapter 1. The reduction of chemical mechanisms is a field unto itself, and is beyond the scope of this discussion.

The detailed mechanism used for most of the simulations in this thesis is designed for methane-air combustion and consists of 46 reactions among 16 species. It is a C1 chemical mechanism, and thus is most appropriate to stoichiometric and lean flames. The larger GRIMech mechanisms use both C1 and C2 chemistry and are perhaps the most detailed mechanisms available for hydrocarbon combustion, but we eschew them in favor of computational efficiency. For stoichiometric and lean flames, the simpler 46-reaction mechanism provides excellent predictions, as reported by Smooke [33]. The mechanism is shown in Table 2-1.

	REACTIONS CONSIDERED			(k = A T**b exp(-E/RT)) A	b	E
1.	CH3+H=CH4			1.90E+36	-7.0	9050.0
2.	CH4+O2=CH3+HO2			7.90E+13	0.0	56000.0
3.	CH4+H=CH3+H2			2.20E+04	3.0	8750.0
4.	CH4+O=CH3+OH			1.60E+06	2.4	7400.0
5.	CH4+OH=CH3+H2O			1.60E+06	2.1	2460.0
6.	CH2O+OH=HCO+H2O			7.53E+12	0.0	167.0
7.	CH2O+H=HCO+H2			3.31E+14	0.0	10500.0
8.	CH2O+M=HCO+H+M			3.31E+16	0.0	81000.0
9.	CH2O+O=HCO+OH			1.81E+13	0.0	3082.0
10.	HCO+OH=CO+H2O			5.00E+12	0.0	0.0
11.	HCO+M=H+CO+M			1.60E+14	0.0	14700.0
12.	HCO+H=CO+H2			4.00E+13	0.0	0.0
13.	HCO+O=OH+CO			1.00E+13	0.0	0.0
14.	HCO+O2=HO2+CO			3.00E+12	0.0	0.0
15.	CO+O+M=CO2+M			3.20E+13	0.0	-4200.0
16.	CO+OH=CO2+H			1.51E+07	1.3	-758.0
17.	CO+O2=CO2+O			1.60E+13	0.0	41000.0
18.	CH3+O2=CH3O+O			7.00E+12	0.0	25652.0
19.	CH3O+M=CH2O+H+M			2.40E+13	0.0	28812.0
20.	CH3O+H=CH2O+H2			2.00E+13	0.0	0.0
21.	CH3O+OH=CH2O+H2O			1.00E+13	0.0	0.0
22.	CH3O+O=CH2O+OH			1.00E+13	0.0	0.0
23.	CH3O+O2=CH2O+HO2			6.30E+10	0.0	2600.0
24.	CH3+O2=CH2O+OH			5.20E+13	0.0	34574.0
25.	CH3+O=CH2O+H			6.80E+13	0.0	0.0
26.	CH3+OH=CH2O+H2			7.50E+12	0.0	0.0
27.	HO2+CO=CO2+OH			5.80E+13	0.0	22934.0
28.	H2+O2=2OH			1.70E+13	0.0	47780.0
29.	OH+H2=H2O+H			1.17E+09	1.3	3626.0
30.	H+O2=OH+O			2.00E+14	0.0	16800.0
31.	O+H2=OH+H			1.80E+10	1.0	8826.0
32.	H+O2+M=HO2+M			2.10E+18	-1.0	0.0
	H2O	Enhanced by	2.100E+01			
	CO2	Enhanced by	5.000E+00			
	H2	Enhanced by	3.300E+00			
	CO	Enhanced by	2.000E+00			
	O2	Enhanced by	0.000E+00			
	N2	Enhanced by	0.000E+00			
33.	H+O2+O2=HO2+O2			6.70E+19	-1.4	0.0
34.	H+O2+N2=HO2+N2			6.70E+19	-1.4	0.0
35.	OH+HO2=H2O+O2			5.00E+13	0.0	1000.0
36.	H+HO2=2OH			2.50E+14	0.0	1900.0
37.	O+HO2=O2+OH			4.80E+13	0.0	1000.0
38.	2OH=O+H2O			6.00E+08	1.3	0.0
39.	H2+M=H+H+M			2.23E+12	0.5	92600.0
	H2O	Enhanced by	6.000E+00			
	H	Enhanced by	2.000E+00			
	H2	Enhanced by	3.000E+00			
40.	O2+M=O+O+M			1.85E+11	0.5	95560.0
41.	H+OH+M=H2O+M			7.50E+23	-2.6	0.0
	H2O	Enhanced by	2.000E+01			
42.	H+HO2=H2+O2			2.50E+13	0.0	700.0
43.	HO2+HO2=H2O2+O2			2.00E+12	0.0	0.0
44.	H2O2+M=OH+OH+M			1.30E+17	0.0	45500.0
45.	H2O2+H=HO2+H2			1.60E+12	0.0	3800.0
46.	H2O2+OH=H2O+HO2			1.00E+13	0.0	1800.0

NOTE: A units mole-cm-sec-K, E units cal/mole

Table 2-1: Smooke-46 chemical mechanism for methane-air combustion.

Chapter 3

Numerical Solution

The evolution of the elemental flame is governed by a set of one-dimensional partial differential equations, as derived in the previous chapter. Difficulty in the numerical solution of these PDEs stems from the inclusion of detailed chemistry. The chemical source terms $\dot{w}_k$ are composites of elementary rate expressions, where each rate expression is a strong, usually exponential, function of temperature. Together, these source terms introduce a wide range of time scales to the governing equations, extending to the order of nanoseconds. Overcoming the stiffness of detailed chemistry has been a long-standing challenge in numerical combustion simulation, one which here necessitated the use of several novel numerical tools.

3.1 Finite-difference Discretization

The governing equations of the elemental flame (Equations 2.32–2.35) must be integrated implicitly, as required by stiffness. A first-order, backward Euler formulation is used, discretizing the time derivatives as follows:

$$\rho\frac{\partial T}{\partial t} = \mathcal{F}\ (T, V, Y_k, \ldots) \rightsquigarrow \rho^{n+1}\frac{T^{n+1} - T^n}{\Delta t} = \mathcal{F}\left(T^{n+1}, V^{n+1}, Y_k^{n+1}, \ldots\right) \quad (3.1)$$

Here and in all subsequent discretizations, the superscript indicates the time layer; the time derivative in the energy equation is used as an example. In contrast to previ-

ous formulations [22], all the governing equations—energy conservation, momentum conservation, species conservation, and continuity—are solved simultaneously.

To prevent the formation of numerical instabilities, convective terms in the species, energy, and momentum conservation equations are discretized with a first-order upwind stencil. This stencil thus depends on the sign of the convective velocity:

$$V_j < 0: \; V\frac{\partial T}{\partial y} \approx V_j \frac{T_{j+1} - T_j}{h_j} \tag{3.2}$$

$$V_j > 0: \; V\frac{\partial T}{\partial y} \approx V_j \frac{T_j - T_{j-1}}{h_{j-1}} \tag{3.3}$$

Here, the subscript represents the point on the spatial grid, while h is the grid spacing: $h_j \equiv y_{j+1} - y_j$. Diffusion terms are approximated to second-order accuracy. Again, the energy equation (2.33) is used as an example:

$$\frac{1}{C_p}\frac{\partial}{\partial y}\left(\lambda\frac{\partial T}{\partial y}\right) \approx \frac{1}{C_{p,j}}\frac{2}{y_{j+1} - y_{j-1}}\left(\lambda_{j+1/2}\frac{T_{j+1} - T_j}{h_j} - \lambda_{j-1/2}\frac{T_j - T_{j-1}}{h_{j-1}}\right) \tag{3.4}$$

The continuity equation (2.35) must be carefully discretized to avoid numerical oscillations in the mass flux profile. Without an appropriate stencil, oscillations are observed during translation of the flame with respect to the spatial grid; susceptibility to oscillations is high since the continuity equation is the only governing equation without physical dissipation. Thus, an upwind discretization is used. The term 'upwind' is written with some qualification, since the continuity equation is not properly a transport equation and $\partial V/\partial y$ is not a convective term per se. Nonetheless, taking the positive sign of $\partial V/\partial y$ to suggest a positive upwind velocity, the following discretization of the continuity equation adds dissipation of the appropriate sign:

$$\frac{\partial \rho}{\partial t} + \frac{\partial V}{\partial y} + \rho U \epsilon = 0 \; \rightsquigarrow$$

$$\frac{\rho_j^{n+1} - \rho_j^n}{\Delta t} + \frac{V_j^{n+1} - V_{j-1}^{n+1}}{h_{j-1}} + \rho_j^{n+1} U_j^{n+1} \epsilon^{n+1} = 0 \tag{3.5}$$

This discretization of $\partial V/\partial y$ prevents direct implementation of the stagnation point boundary condition, Equation 2.28. Instead, a boundary value on the mass flux V

must be chosen at $y = -\infty$. The boundary value is arbitrary provided that it is large enough for a flame to stabilize at a lower mass flux, since V decreases in the direction of the stagnation point. If the boundary value is too large, on the other hand, the flame (or for that matter, the stagnation point) may not fall within the computational domain. The boundary value can thus be set to any reasonable number based on the size of the computational domain and the strain rate. The solution to the problem matches the mass flux profile to the flame location, as reflected in the profiles of T, Y_k, ρ, and U. In computations with changing strain rate, the boundary condition on V must be updated periodically, a process detailed in §3.4.2.

Spatial discretization of the governing equations is performed on a non-uniform adaptive grid. Non-uniform grid spacing permits a greater clustering of grid points in regions where spatial gradients are strong, thus ensuring adequate resolution through the reaction-diffusion zone; a fine grid resolution tends to offset the fact that convective discretizations are only first-order accurate. Grid points are more sparsely spaced away from the flame, in regions of constant gradient. This non-uniform allocation of grid points provides accuracy without sacrificing computational efficiency.

As the flame translates in space or as its internal structure changes, adaptivity of the grid becomes important. Several criteria for grid resolution are enforced at the end of each time step, and where these criteria are not met, grid points are added or removed appropriately. First, the gradient of each scalar must be adequately resolved, relative to its range:

$$|\varphi_{j+1} - \varphi_j| < \alpha \left| \max_j \varphi - \min_j \varphi \right| \tag{3.6}$$

Here, φ is chosen to include all the dependent variables (T, Y_k, U, and V) as well as each chemical source term $\dot{w}_k$; α is a tolerance parameter on the order of 0.1. Second gradients are subject to an analogous criterion:

$$\left| \left(\frac{\partial \varphi}{\partial y} \right)_{j+1} - \left(\frac{\partial \varphi}{\partial y} \right)_j \right| < \beta \left| \max_j \left(\frac{\partial \varphi}{\partial y} \right) - \min_j \left(\frac{\partial \varphi}{\partial y} \right) \right| \tag{3.7}$$

The final criterion forces the grid to be relatively uniform:

$$\gamma < \frac{h_j}{h_{j-1}} < 1/\gamma \tag{3.8}$$

Linear interpolation is used to calculate the value of the dependent variables at any new grid point.

At the end of each time step, the thickness of the flame's temperature profile is compared to the distance from each boundary to the nearest end of the flame. If the flame comes to within two thermal thicknesses of the boundary, the computational domain is extended and values of each dependent variable are extrapolated to the new grid points. This criterion for grid extension is most important on the products side of a premixed flame, where the boundary conditions expect the mixture to have reached equilibrium, with all spatial gradients in T, Y_k, and U falling to zero.

The time step for integration is constant, typically chosen in the range of 1–10 μs. At each time step, discretization reduces the governing PDEs to a set of nonlinear algebraic equations. The nonlinear system can be written as:

$$F(x) = 0, \quad F: \mathbb{R}^n \rightarrow \mathbb{R}^n \tag{3.9}$$

The output of the function F is a column vector containing residuals of the discretized governing equations, while x is the solution vector, containing profiles of each fundamental variable, Y_k, T, U, and V. The organization of the values within these column vectors is important, as it affects the bandwidth and structure of the Jacobian matrix,

$F'_{ij} \equiv \partial F_i / \partial x_j$. Variables and residuals are thus grouped by grid point:

$$x = \begin{pmatrix} \vdots \\ Y_{(k=1),\,j} \cdots Y_{(k=K),\,j} \\ T_j \\ U_j \\ V_j \\ Y_{(k=1),\,j+1} \cdots Y_{(k=K),\,j+1} \\ T_{j+1} \\ U_{j+1} \\ V_{j+1} \\ \vdots \end{pmatrix} \tag{3.10}$$

$$F = \begin{pmatrix} \vdots \\ res_{spec(k=1),\,j} \cdots res_{spec(k=K),\,j} \\ res_{energy,\,j} \\ res_{mntm,\,j} \\ res_{cont,\,j} \\ res_{spec(k=1),\,j+1} \cdots res_{spec(k=K),\,j+1} \\ res_{energy,\,j+1} \\ res_{mntm,\,j+1} \\ res_{cont,\,j+1} \\ \vdots \end{pmatrix} \tag{3.11}$$

Here, $res_{energy,\,j}$ denotes the residual of the energy conservation equation discretized at grid point j; similar notation applies to the residuals of the conservation equation for species k ($res_{spec(k),\,j}$), the momentum conservation equation ($res_{mntm,\,j}$), and the continuity equation ($res_{cont,\,j}$).

3.2 Inexact Newton Method

The most basic means of solving nonlinear equations is Newton's method. The solution is approached by iteration; a linear model is constructed at each trial solution to yield a step, or correction, towards a more accurate solution. For a nonlinear system of equations as in (3.9), the Newton step is given by

$$F'(x_k)s_k = -F(x_k) \tag{3.12}$$

where x_k is the current approximate solution and s_k is the step towards the next solution, $x_{k+1} = x_k + s_k$. As defined in the previous section, $F'(x_k)$ is the Jacobian computed at x_k, $F'_{ij} \equiv \partial F_i / \partial x_j$.

Newton's method converges quadratically in the neighborhood of a solution, a desirable feature when the trial solution is accurate. Far away from a solution, however, Newton's method is not robust, converging poorly if at all. Directly solving Equation 3.12 for a Newton step—a computationally expensive undertaking in any large scale problem—is not effective in this situation. Replacing the Newton condition of Equation 3.12, we introduce the more flexible *inexact Newton condition*:

$$\|F(x_k) + F'(x_k)s_k\| \leq \eta_k \|F(x_k)\| \tag{3.13}$$

This modification of the Newton equation is at the core of the Inexact Newton Backtrackng (INB) method, developed by Eisenstat and Walker [7].

The key parameter in Equation 3.13 is η_k, known as the forcing term. The inexact Newton condition essentially restates the exact Newton conditon from the perspective of an iterative linear solver. An iterative method is used to find an approximate solution to (3.12), and η_k specifies the tolerance to which this solution (s_k) is found. For η_k equal to zero, the Newton condition is solved exactly, reducing Equation 3.13 to Equation 3.12, while as η_k approaches 1, computational effort falls to zero.

Proper specification of η_k can vastly enhance efficiency and convergence of the nonlinear solver. Far away from a solution, where the linear model of Equation 3.12

may poorly describe the nonlinear surface of the function F, it makes little sense to calculate each Newton step exactly. Doing so is computationally expensive and may result in little or no progress toward a solution; indeed, a less accurate solution of (3.12) may be more effective in reducing $\|F\|$. The forcing term is thus chosen close to 1. If the linear model becomes accurate, however, a precise Newton step is likely to provide fast reduction in $\|F\|$; the forcing term is thus chosen close to zero. Explicit formulas governing the choice of η_k at each iteration will be given, but first let us outline the entire Inexact Newton Backtracking algorithm:

Algorithm 3.1 (Inexact Newton Backtracking Method)

Let x_o, $\eta_{max} \in [0,1)$, $t \in (0,1)$, *and* $0 < \theta_{min} < \theta_{max} < 1$ *be given.*

For $k = 0, 1, \ldots,$ until convergence*:*

Choose initial $\eta_k \in [0, \eta_{max}]$ *and* s_k *such that*

$$\|F(x_k) + F'(x_k)s_k\| \leq \eta_k \|F(x_k)\|.$$

While $\|F(x_k + s_k)\| > [1 - t(1 - \eta_k)] \|F(x_k)\|$ *do:*

Choose $\theta \in [\theta_{min}, \theta_{max}]$.

Update $s_k \longleftarrow \theta s_k$ *and* $\eta_k \longleftarrow 1 - \theta(1 - \eta_k)$.

Set $x_{k+1} = x_k + s_k$.

This algorithm augments the inexact Newton condition with a globalization known as *safeguarded backtracking.* Sufficient reduction in the norm of F is enforced at the 'while' loop; if the step s_k of the inexact Newton condition does not sufficiently reduce $\|F\|$, the step is reduced by a scalar factor θ, essentially 'backtracking' along the search direction. Backtracking continues until the condition on $\|F\|$ is met, for in a sufficiently small neighborhood of the trial solution x_k, the linear model must indicate the correct downward path; the Newton equation is consistent. The backtracking process is considered 'safeguarded' because limits are placed on the choice of θ, and it is known as a 'globalization' because it vastly improves the domain of convergence of Newton's method. Indeed, in exact arithmetic, the INB algorithm is guaranteed to converge from an arbitary initial guess unless x_k has no limit points or x_k only has limit points at which F' is singular [7].

As described above, the forcing term η_k is updated at each iteration to reflect the accuracy of the local linear model. Two schemes that provide fast local convergence while minimizing oversolving are given by Pernice and Walker [19]. For the first, we select $\eta_o \in [0, 1)$ and choose subsequent values of η_k as follows:

$$\eta_k = \frac{|\|F(x_k)\| - \|F(x_{k-1}) + F'(x_{k-1})s_{k-1}\||}{\|F(x_{k-1})\|}, \quad k = 1, 2, \ldots \tag{3.14}$$

The second scheme updates η_k based on the norm reduction of the previous Newton iteration, a more indirect measure of the accuracy of the local linear model:

$$\eta_k = \gamma \left(\frac{\|F(x_k)\|}{\|F(x_{k-1})\|} \right)^{\alpha}, \quad k = 1, 2, \ldots \tag{3.15}$$

The scaling γ is chosen in $[0, 1]$ and the exponent α is chosen in $(1, 2]$.

In our implementation of the INB method, convergence is declared when $\|F(x_k)\|_2$ or $\|F(x_k)\|_\infty$ falls below a specified tolerance, usually 10^{-9}. Equation 3.14 is typically used to specify the forcing terms, with $\eta_o = 0.5$. The remaining parameters are adjusted arbitrarily to enhance convergence.

3.3 Krylov Subspace Iterative Solver

Iterative solution of the Newton equation (3.12) is a rather large scale problem. For a typical grid of 150 points and a detailed mechanism of 16 species, the Jacobian matrix F' is of dimension $m \approx 3000$. Given that the Newton equation is solved repeatedly in the course of a single time step, an efficient linear iterative method is essential to the performance of the code. Here we turn to a modern class of iterative methods known as Krylov subspace methods, and we develop preconditioners to accelerate their convergence.

3.3.1 BiCGSTAB

Krylov subspace methods are based on the idea of projecting an m-dimensional problem onto a lower-dimensional Krylov subspace [36]. For a linear system $Ax = b$, a Krylov subspace of dimension n is defined as follows:

$$\mathcal{K}_n = \langle b, Ab, \ldots, A^{n-1}b \rangle \tag{3.16}$$

At each iteration, the trial solution x_n is chosen from the subspace $\mathcal{K}_n$; iteration increases the size of the Krylov subspace and thus the accuracy of the solution. GMRES (*G*eneralized *M*inimum *Res*idual) is probably the simplest and best-known Krylov method, and its workings are illustrative: At each step, Arnoldi iterations construct an orthonormal basis for $\mathcal{K}_n$. A least-squares approximation then finds the $x_n \in \mathcal{K}_n$ that minimizes the norm of the residual $b - Ax$.

In our implementation of the INB algorithm, we use a variant Krylov subspace method known as BiCGSTAB—*Bi*-*C*onjugate *G*radients *Stab*ilized. The details of this method are more complex, and are left better-described elsewhere [36, 10, 30]. BiCGSTAB is based on Lanczos iteration, which, in contrast to the Arnoldi iterations of GMRES, uses a three-term recurrence relation to construct an orthonormal basis for $\mathcal{K}_n$. BiCGSTAB does not strictly minimize the residual norm at each iteration, and its convergence is not monotonic. However, it requires less storage space, and in our experience, provides greater numerical stability.

An important attribute of Krylov subspace methods is that they do not operate directly on the matrix A. All that is required is matrix-vector products Ax, making it simple to design procedures that exploit the sparsity of A. For a matrix of dimension m with only ν nonzero entries per row, one can easily compute Ax in $O(\nu m)$ rather than $O(m^2)$ operations. In the context of the INB algorithm, our matrix A is the Jacobian, F', and a finite-difference formula is used to calculate the product of F' with an arbitrary vector v:

$$F'(x_k)v \approx \frac{1}{2\delta}\left[F(x_k + \delta v) - F(x_k - \delta v)\right] \tag{3.17}$$

The scalar perturbation δ is chosen as follows:

$$\delta = \frac{\left[\left(1 + \|x_k\|\right)\epsilon_{mach}\right]^{1/3}}{\|v\|} \tag{3.18}$$

where ϵ_{mach} denotes machine epsilon.

3.3.2 ILUTP Preconditioning

The inclusion of detailed chemistry in the governing equations (2.32–2.35) creates scalar entries of the Jacobian that span several orders of magnitude relative to one another. Stiffness on the continuous scale thus manifests itself as an extremely ill-conditioned linear algebra problem. Indeed, the condition number $\kappa(F')$ is typically on the order of 10^9. The convergence properties of BiCGSTAB and other Krylov methods are not completely understood, but it is known that they hinge on the eigenvalue or singular value distribution of the matrix. As a rule of thumb, closely and uniformly distributed eigenvalues produce fast convergence, and an ill-conditioned matrix has a spectrum that is quite the opposite. The question then arises of how to improve the properties of our Jacobian matrix so that BiCGSTAB converges rapidly? In principle, a Krylov subspace method must converge in $n \ll m$ steps if it is to be useful. The answer lies in preconditioning—subjecting the matrix to operations that improve its eigenvalue spectrum from the perspective of the Krylov subspace solver.

The basic procedure of preconditioning is outlined as follows.[1] The linear system $Ax = b$ is replaced by two equations:

$$AM^{-1}y = b \tag{3.19}$$

$$Mx = y \tag{3.20}$$

The Krylov subspace solver is applied to the first equation, while x is calculated from the second. To accelerate convergence of the Krylov solver, M is chosen so

[1] Actually, this is just *right* preconditioning. A preconditioner may also be applied on the left ($M^{-1}Ax = M^{-1}b$), or on both sides, to preserve hermitian positive definiteness ($\left[C^{-1}AC^{-*}\right]C^{*} = C^{-1}b$).

that AM^{-1} is not too far from normal and its eigenvalues are clustered; AM^{-1} is the well-behaved matrix that the Krylov solver "sees." On the other hand, M must also be chosen so that Equation 3.20 is simple to solve. The preconditioner M must lie somewhere between A and I on a spectrum of approximation; choosing $M = A$ or $M = I$ would render Equation 3.20 or Equation 3.19, respectively, equivalent to the original ill-conditioned problem.

The right preconditioner implemented here is based on the idea of *incomplete LU factorization*, ILU for short. An exact LU factorization of a sparse matrix like F' produces two dense matrices L and U; the replacement of zero entries in F' with nonzero entries in L and U is known as fill-in. Suppose, however, that fill-in were prevented, that $\tilde{L}$ and $\tilde{U}$ could have nonzero entries only where F' was nonzero. Then, $\tilde{L}$ and $\tilde{U}$ are the incomplete LU factors of F', and

$$M = \tilde{L}\tilde{U} \approx F' \tag{3.21}$$

becomes a useful preconditioner.

Several refinements of ILU factorization have been developed by Saad [30] and published in his SPARSKIT sparse matrix toolkit. Using this package, we implement an ILUTP preconditioner, a more accurate ILU factorization that allows some fill-in. ILUTP preconditioning regulates fill-in in L and U on the basis of two parameters: one, called *lfil*, is the absolute number of fill-in elements that are allowed in each row of L or U; the second, called *droptol* is threshold value below which a potential fill-in element is set to zero. The ILUTP approach also provides for pivoting, in which the original matrix is permuted to insure diagonal dominance. Details of the ILUTP algorithm are more fully described elsewhere [30].

To improve the stability of the factorization process, we scale each column of the matrix by its 1-norm prior to computing the preconditioner. The entire preconditioning process can now be summarized as follows, where A is understood to be the Jacobian F':

$$ASP \approx LU \equiv M \tag{3.22}$$

$$Ax = b \longrightarrow$$

$$ASP(LU)^{-1}y = b \tag{3.23}$$

$$S^{-1}P^{-1}LUx = y \tag{3.24}$$

S is a diagonal matrix containing the column-scaling parameters and P is the permutation matrix. The Jacobian is scaled and permuted, then factored into L and U. The original linear problem then consists of solving (3.23) and (3.24). BiCGSTAB is applied to Equation 3.23; in Equation 3.24, S and P are inverted by inspection, and back-substitution is used to invert L and U.

Implementing this preconditioning scheme in the context of the INB algorithm is relatively simple. The preconditioning factors L, U, S, and P are computed and stored at the start of each Newton iteration. The BiCGSTAB algorithm requires only matrix-vector products, specifically the product of $ASP(LU)^{-1}$ with arbitrary vectors z. Equation 3.24 is thus used to compute $v = SP(LU)^{-1}z$, and the output v is sent to Equation 3.17. Applying the preconditioner thus consists of repeatedly inverting Equation 3.24. In practice, the preconditioning factors need not be computed at the start of *each* Newton iteration, as the Jacobian may not change significantly, and preconditioning is, after all, approximate. The optimal frequency for updating the preconditioner rests on a balance of computational times: the additional time required to recalculate L, U, S, and P versus the time this saves by speeding the convergence of BiCGSTAB.

In contrast to the matrix-free formulation of the Krylov subspace solver, computing the preconditioner by the methods described in this section requires an explicit Jacobian. At each preconditioner update, entries of the block-tridiagonal Jacobian are constructed according to the definition, $F'(x_k)_{ij} \equiv \partial F(x_k)_i / \partial x_{k,j}$. Most of these derivatives can be computed analytically, but those involving chemical source terms are computed via finite-difference approximation:

$$\frac{\partial \dot{w}_k}{\partial Y_{k*}} = \frac{\dot{w}_k(T, Y_1, \ldots, Y_{k*} + \delta Y_{k*}, \ldots, Y_K) - \dot{w}_k(T, Y_1, \ldots, Y_{k*}, \ldots, Y_K)}{\delta Y_{k*}} \tag{3.25}$$

where δ is usually chosen around 10^{-3}; here the derivative with respect to species mass fraction was chosen as an example. To compute derivatives of $\dot{w}_k$ analytically would entail decomposing the chemical rate expressions within CHEMKIN—a difficult undertaking—and would compromise the modularity of the code with respect to kinetic schemes. In addition, derivatives of the transport coefficients with respect to T or Y_k cannot be computed easily, since they involve polynomial approximations within CHEMKIN for C_p. These derivatives are omitted from the explicit Jacobian; the resulting inaccuracy is generally insignificant, since L and U are approximate factors.

3.4 Initialization Conditions

Despite the robust convergence properties of the INB method, it will not converge quickly from a completely arbitrary profile. At every time step, the Newton solver requires a starting point for its iterations, an initial guess x_o. Ingenuity in creating these initialization conditions can yield large computational savings. We analyze this process in two cases: creating a starting condition for the code at $t = 0$, and selecting the inital guess at each time step while the code is running, i.e., for $t > 0$.

3.4.1 Starting Case

When applying the elemental flame code to a new chemical mechanism or a new flame configuration, an initial solution vector is assembled to approximate the expected flame structure as closely as possible. This guess is both x at the $n = 0$ time step and the initial guess for $x^{n=1}$. A reasonable procedure for creating such an initial guess is as follows: Hyperbolic tangent functions are used to approximate $T(y)$, $U(y)$, and the mass fraction profiles of major species. Gaussians are used to approximate the profiles of minor species. In a premixed flame, an equilibrium code such as STANJAN provides product-side boundary conditions on T and Y_k, and in all cases, a steady-state version of the continuity equation (2.35) is integrated to find V. The thickness and height of each profile must be estimated based on knowledge of the

kinetic mechanism and of typical flame structure at the desired strain rate.

Clearly, this ad hoc scheme cannnot predict the flame structure very closely. To create a more accurate starting condition for the elemental flame, the initial guess is subjected to a *continuation* scheme for gradually introducing the chemical source terms. Chemistry is the root of stiffness in the governing equations, and thus is the primary cause of difficult convergence. The continuation scheme places damping terms—arbitrary scalar factors θ—in front of the chemical source terms in the energy and species equations (2.33 and 2.32), converting the elemental flame into a weakly-reacting or non-reacting mixture as follows:

$$\rho\frac{\partial Y_k}{\partial t} + V\frac{\partial Y_k}{\partial y} - \frac{\partial}{\partial y}\left(\frac{1}{Le_k}\frac{\lambda}{C_p}\frac{\partial Y_k}{\partial y}\right) - \theta\dot{w}_k W_k = 0 \tag{3.26}$$

$$\rho\frac{\partial T}{\partial t} + V\frac{\partial T}{\partial y} - \frac{1}{C_p}\frac{\partial}{\partial y}\left(\lambda\frac{\partial T}{\partial y}\right) - \theta\sum_k \frac{\dot{w}_k h_k}{C_p} = 0 \tag{3.27}$$

The initial guess is used to start the code in a weakly-reacting form, and as time integration proceeds, the damping terms θ are gradually increased to unity. Once the solution vector reaches steady-state, it becomes a physically accurate starting case.

The continuation scheme typically begins with damping terms on the order of 10^{-3} and brings them to 1.0 in about 10 ms of integration. Precise values depend on the stiffness of the kinetic scheme, the accuracy of the initial guess, and the flame time scale.

3.4.2 Mass Flux Projection Method

When $t > 0$, creating the initial guess for the solution vector at each time step is much simpler; the inital guess at $t = n+1$ is just x^n. This procedure creates difficulty in the case of unsteady strain, however. Recall that to aid in discretization, the boundary condition on V is imposed at $y = -\infty$. The strain rate ϵ can easily vary one or two orders of magnitude in a given simulation, however; such a change in strain, with a fixed boundary value on the mass flux through the flame, causes the flame to translate rapidly with respect to the grid. The flame nears the boundary of the

computational domain, and successive regriddings become necessary. This outcome is not only cumbersome, but computationally taxing; when the flame translates quickly, x^n is a poor guess for x^{n+1}.

To avoid this situation while retaining the boundary condition $V(y = -\infty)$, we implement a projection method to update the mass flux profile in the case of unsteady strain. At the start of time step $n + 1$, an initial guess for V^{n+1} is obtained by integrating the continuity equation with ϵ^{n+1}, U^n, and ρ^n:

$$\frac{\rho_j^n - \rho_j^{n-1}}{\Delta t} + \frac{V_j^{n+1,\,guess} - V_{j-1}^{n+1,\,guess}}{h_{j-1}} + \rho_j^n U_j^n \epsilon^{n+1} = 0 \tag{3.28}$$

In one step, this projection updates the boundary value on V at $y = -\infty$ and generates a new guess for V^{n+1}. Updating the boundary value on V minimizes flame translation for fast convergence.

Chapter 4

Steady-State Validation

The numerical solution of the elemental flame assembles a number of novel mathematical techniques. Before the resulting code is applied to problems of flow and mixture inhomogeneity, it is important to model a standard, well-understood flame configuration and check the accuracy of the results, thus validating the numerical methods, the transport model, and the underlying formulation of the elemental flame. This chapter presents a direct comparison of the elemental flame code with Sandia's steady-state OPPDIF (Opposed Flow Diffusion Flame) solver; both codes are used to compute the detailed structure of a strained, premixed methane-air flame.

4.1 OPPDIF Formulation

OPPDIF is designed to compute the steady-state structure of an axisymmetric flame between two opposed nozzles, as shown in Figure 4-1. Though its name suggests otherwise, OPPDIF models reacting flow between two jets of arbitrary composition; thus premixed combustion may be represented in both single-flame and two-flame configurations. The flow conditions are defined by the distance between the two nozzles and the mass flux of each species through each nozzle, along with the density of each stream. The flow leaving each nozzle is divergence-free, i.e., the radial velocity component at the nozzle equals zero. A similarity solution reduces this two-dimensional flow to a single dimension, along the centerline. The resulting governing equations

form a two-point boundary value problem. To satisfy the radial momentum equation, the radial pressure gradient $\frac{1}{r}\frac{\partial p}{\partial r}$ is constant across the domain; it must be computed as an eigenvalue. Further detail on this formulation may be found in [15].

The OPPDIF formulation differs significantly from that of the elemental flame, which imposes an outer flow solution for stagnation flow from a point source at minus-infinity onto a compressible boundary layer. The elemental flame uses a single strain rate, useful in parametrizing solutions for flamelet modeling, but *imposes* no length scale on the problem. (The only length scale is the flame thickness, and this value is calculated, not imposed.) In contrast, the OPPDIF formulation imposes a length scale—the nozzle separation—but does not define a characteristic strain; a strain must be backed out of the final solution. This formulation is better suited to modeling the experimental configurations actually used to study strained laminar flames, which physically do create a stagnation plane between opposed jets of uniform flow. A detailed discussion contrasting one- and two-parameter formulations for the strained laminar flame may be found in [34, 12].

The species transport model used in OPPDIF is more detailed than that of the elemental flame (see §2.3.1). At each point in the domain, OPPDIF computes diffusion velocities by a multicomponent formulation; thermal diffusion velocities are not neglected. For the purposes of comparison, both OPPDIF and the elemental flame code are run with Smooke's 46-reaction C1 mechanism (Table 2-1), however. The kinetic scheme has too important an effect on flame structure not to be conserved in the comparison.

OPPDIF uses a finite-difference discretization on a uniform grid, reserving upwind differencing for convective terms, as in the elemental flame. Several iterations are necessary to obtain a well-resolved solution, however. OPPDIF is first made to converge on a coarse grid, then this solution is used as the starting condition on a finer grid. Successively finer grids, typically three or four, are introduced until the reaction zone of the flame is clearly resolved.

4.2 Comparison of Results

Though OPPDIF does not model a true stagnation point flow, the flow field local to the stagnation plane approaches that of a stagnation point. The strain rate effectively applied to the flame is found by examining the axial velocity profile immediately ahead of the flame, on the reactants side. Before any expansion due to burning has occurred, the "cold" hydrodynamic strain is obtained from the usual relation:

$$\epsilon = -\frac{\partial v}{\partial y} \tag{4.1}$$

Figure 4-2 shows the velocity profile v for both an OPPDIF solution and the elemental flame, where both codes have been used to compute an axisymmetric premixed flame at a strain rate of 100 s^{-1}. The common centerline coordinate has been defined such that both flames reach their stagnation point at $y = 0$. Note that the slopes $\partial v/\partial y$ are identical immediately ahead of the flame, where expansion is then manifested as a sharp rise in axial velocity. The strain rate of 100 s^{-1} was imposed *a priori* on the elemental flame, but achieved through an appropriate choice of nozzle velocities and nozzle separation for the OPPDIF flame.

Of course, the strain fields of the two flames cannot match over the entire domain. The strain rate in the OPPDIF flame must equal zero at the nozzles, where flow is divergence-free, and rise towards the center of the domain due to both expansion within the flame and hydrodynamic, stagnation point, effects. This expectation is borne out in Figure 4-3, where the dimensionless U of the elemental flame is plotted along the common centerline coordinate together with a U for the OPPDIF solution. The equivalent U for the OPPDIF solution is defined as follows:

$$U = \frac{1}{\epsilon}\left(\frac{u}{r}\right)_{r=0} \tag{4.2}$$

where ϵ is our reactants-side strain, 100 s^{-1}.

Now let us examine the temperature and species profiles through the flame region. Figure 4-4 shows temperature and selected major species in both flames, with the

heat release rate in the elemental flame plotted for reference. In this plot and in subsequent plots of flame structure, the OPPDIF flame has been shifted with respect to its coordinate so that it lies directly on top of the elemental flame; a point along the rise of each temperature profile was used to select the appropriate translation. Because of differences in the flow fields of the two flames, the elemental flame sits further from the stagnation point. This does not factor negatively in our comparison; it is the *local* structures and the burning velocities of the flames that we expect to agree.

Indeed, close agreement is observed in the temperature and major species profiles of the OPPDIF solution and the elemental flame. The temperature profile is characteristic of the premixed flame: a fast rise in the peak reaction zone, followed by a slower rise as CO oxidation proceeds. Figure 4-5 extends the comparison to selected minor species. Again, close agreement of profile shape, peak value, and peak location is observed between the two models. The peak in Y_{CH_2O} occurs ahead of the peak in Y_{OH}, since CH_2O is formed earlier in the breakdown of methane. Small and persistent differences in species mass fraction on the products side of the flame may be due to the fact that the products stream composition in the OPPDIF flame deviated slightly from equilibrium.

In sum, the steady-state flame structure predicted by the elemental flame code matches well with that of a well-benchmarked model. Differences in the profiles can be attributed to the distinct flow fields of the two flames, as well as differences in the transport models and in grid spacing. It is significant, particularly in the context of the next chapter, to note that detailed agreement between combustion in the pure stagnation point flow and combustion in the more experimentally realistic opposed-jet flow was obtained by matching strains at the reactants-side leading edge of the flame.

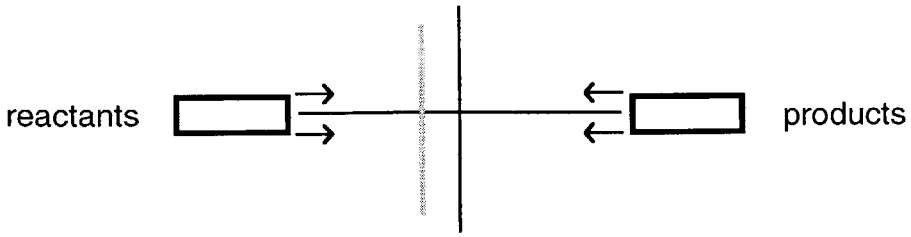

Figure 4-1: Flow configuration modeled by OPPDIF.

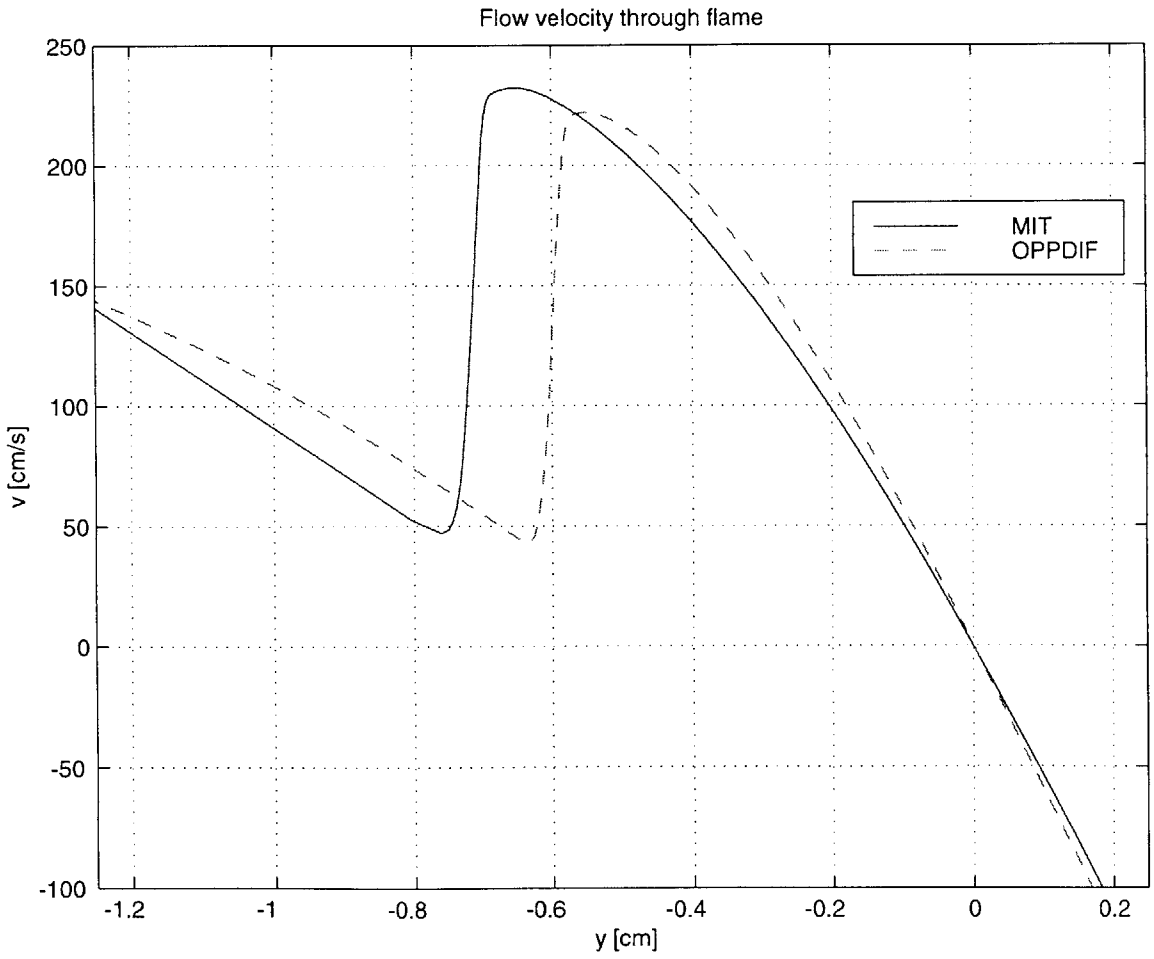

Figure 4-2: Flow velocity through the flame, elemental flame code vs. OPPDIF.

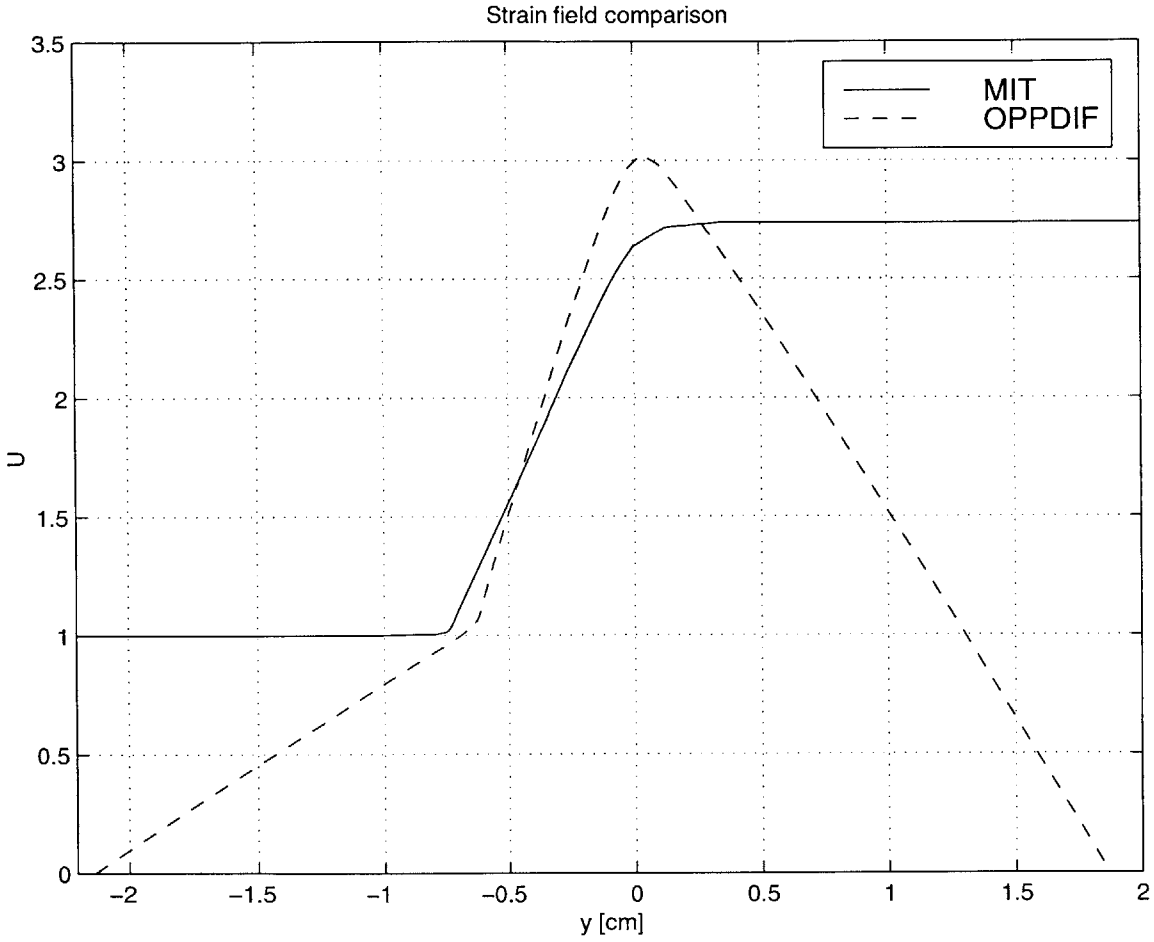

Figure 4-3: Distribution of effective strain, elemental flame code vs. OPPDIF.

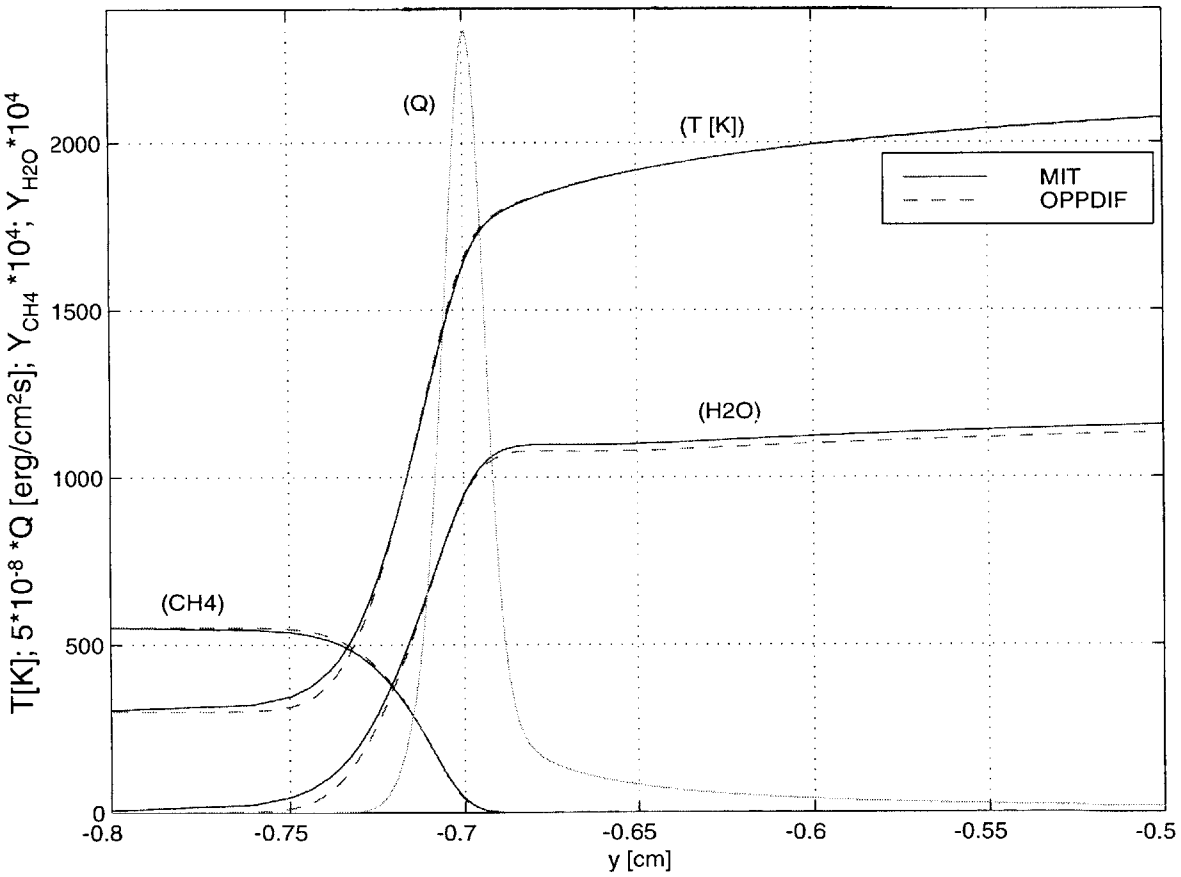

Figure 4-4: Temperature and major species profiles in the flame region, elemental flame code vs. OPPDIF.

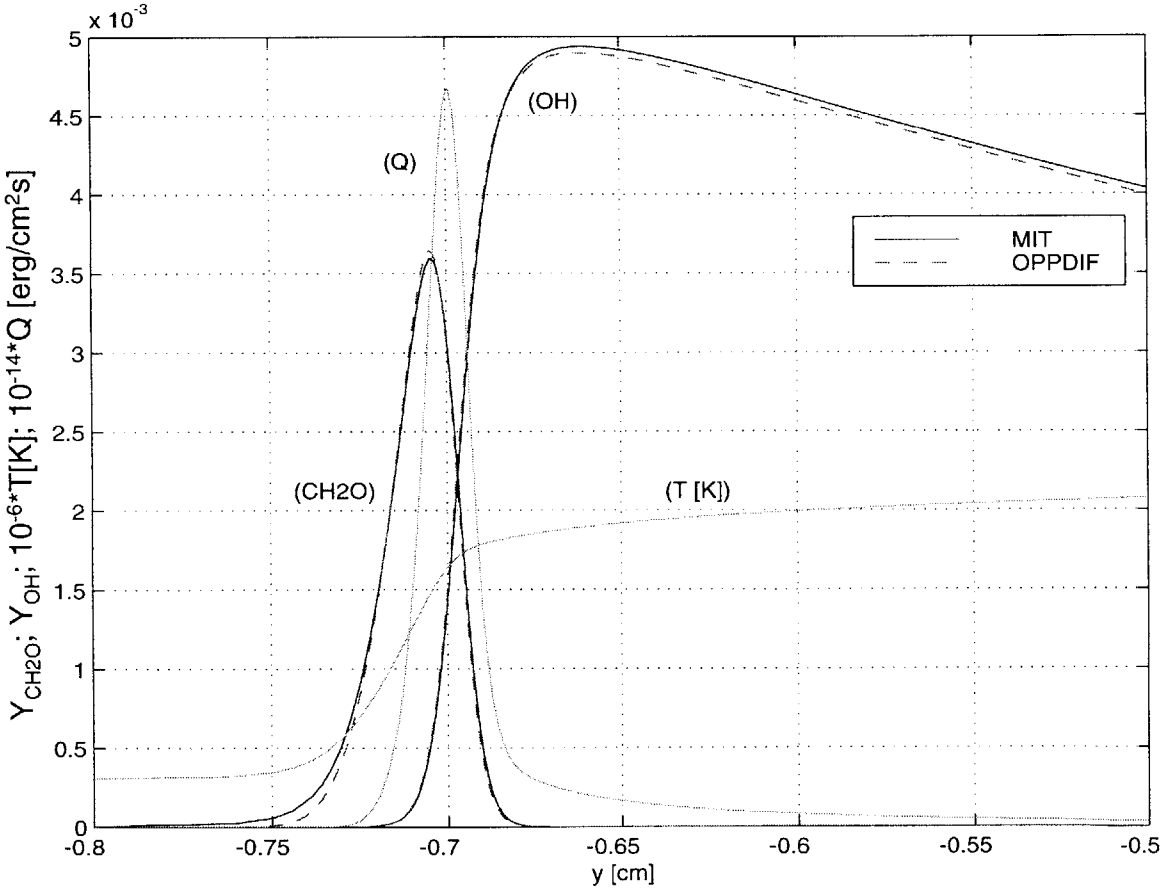

Figure 4-5: Minor species profiles in the flame region, elemental flame code vs. OPPDIF.

Chapter 5

Unsteady Applications

Our focus now returns to the modeling of flow and mixture inhomogeneities. The combustion zone model developed in the preceding chapters is used to examine and expand upon the fundamental unsteady interactions presented in Chapter 1. For clarity, two broad regimes of unsteadiness are treated in separate examples. The first, unsteady variation in equivalence ratio, is presented in terms of the burning of a stratified mixture. The second, unsteady variation in strain, is set in the environment of two-dimensional premixed turbulent combustion: the elemental flame is used to model the burning and structure of a flame surface interacting with a vortex. Because this example effectively tests the ability of a subgrid model to capture a complex turbulent interaction, its analysis holds important implications for the flame embedding technique described in §1.1.

5.1 Burning in a Stratified Mixture

Fast temporal or spatial stratification of a reacting mixture is present in numerous practical phenomena. One of these phenomena is combustion instability, as described in §1.3; another is burning in a direct-injection engine, where the equivalence ratio of the mixture decreases away from the fuel injection port. The goal of this section is to develop a computation that captures the essential features of both of these phenomena, one that answers the following question: how does a temporal change in

ϕ on the order of a flame time scale affect flame structure and burning?

We begin by choosing a strain rate of 300 s^{-1}, a reasonable value for burning in an internal combustion engine [38]. To simulate propagation through a stratified mixture, a change in equivalence ratio from 1.0 to 0.6 is imposed on the reactants stream. Temporal and spatial stratification are rendered equivalent by the Lagrangian frame of the elemental flame; the model simply follows the flame surface as new mixture is encountered.

In the elemental flame model, control of the reactants stream composition comes from the boundary condition on Y_k at $y = -\infty$. An imposed $\phi(t)$ at this boundary will not produce the same change $\phi(t)$ at the flame, however. The flame typically sits some distance away from the edge of the computational domain, so changes in ϕ at the boundary will be subject to a propagation delay as they travel to the flame; during this propagation, the change in ϕ will also be smoothed out via diffusion. The stagnation flow geometry thus makes it difficult to impose an exact $\phi(t)$ on the flame. Fortunately, there is no restriction on the location of the reactants-side edge of the computational domain. To impose a $\phi(t)$ at the flame, the computational domain is resized so that the $y = -\infty$ boundary occurs precisely at the flame's leading edge, thus avoiding the difficulties of propagation delay and its associated diffusion. The leading edge of the flame is defined at the initial rise of the temperature profile. This shortened computational domain can be seen in Figures 5-4 through 5-7.

A second challenge in modeling propagation of the strained flame lies in defining the composition of the products stream. The choice of products-side boundary condition is aided by two physical interpretations: If the products mixture behind the propagating flame is well-mixed, then its composition will not change appreciably during a perturbation in ϕ. This leads to constant boundary conditions on T and Y_k at $y = \infty$, corresponding to, for instance, the products of combustion at $\phi = 1.0$. For reasons that will become clear in §5.1.2, this case is known as the back-supported flame. If, on the other hand, the products mixture is not well-mixed—if it is itself stratified—then the products-side of the flame will be affected only by the instantaneous products of burning. Now the products stream composition must be updated

to reflect the changing reactants-side ϕ; such a flame is deemed to lack back-support.

5.1.1 Dynamic Effect of Equivalence Ratio Variation

Before investigating differences in burning with and without back-support, we focus on the dynamic effect of equivalence ratio variation—how a flame responds to changing ϕ, and how the time scale of this change affects the response. Figure 5-1 shows the heat release rate histories $\dot{Q}(t)$ of two back-supported flames, both subject to the same absolute change in ϕ, as chosen in the discussion above ($\phi = 1.0 \longrightarrow \phi = 0.6$). The solid line corresponds to a linear change in ϕ over a 10 ms period, while the dashed line results from a linear change in ϕ over 2 ms. As expected, both flames reach the same steady-state rate of heat release. For reference, the linear changes in ϕ are plotted on the same scale.

The heat release rate $\dot{Q}(t)$ corresponding to the faster change in ϕ exhibits a greater degree of unsteadiness than its slower counterpart. At the end of the 2 ms change, $\dot{Q}$ has traversed only 40% of its total range; this behavior is not surprising, since 2 ms is approximately a flame time scale. The asterisks in Figure 5-1 represent the steady-state heat release rates corresponding to the same 2 ms change in ϕ, underscoring the fact that the response of the flame to this fast change in ϕ is not steady-state. The heat release rate corresponding to the 10 ms change in ϕ, however, is more quasi-steady; at the conclusion of the ϕ change, only a 10% correction in heat release rate is observed.

5.1.2 Back-support of the Elemental Flame

Updating the composition of the products stream for the non-back-supported flame presents difficulties similar to those encountered in updating the composition of the reactants stream. The flame ordinarily sits far from the products-side boundary, leading to propagation delay and diffusion of the mixture conditions imposed at the products stream. To avoid these problems, the $y = \infty$ boundary cannot be placed arbitrarily, however; consistency with respect to the boundary conditions (Equations 2.29–2.30)

dictates that the computational domain must extend to the point where gradients on U relax to zero. Here, then, is where the mixture boundary conditions are imposed. Based on an interpolation table of equilibrium values for combustion at a given reactants-side ϕ, T and Y_k are updated[1] to reflect the appropriate stream of burned products.

How to time these updates of the products mixture is yet another matter. The mixture should reflect the instantaneous products of burning, but dynamic effects insure that the instantaneous burning is not determined by the current reactants-side ϕ. A reasonable, though approximate, solution to this problem is constructed as follows. The composition of the products stream should reflect burning at an equivalence ratio—call this ϕ_b—equal to the equivalence ratio ϕ_r imposed on the reactants side of the flame *one flame time scale earlier*. For simplicity, we choose a fixed flame time scale, here equal to 2 ms, though in reality the flame time scale will itself change with ϕ_r and ϕ_b.

Using this construction, the effect of back-support is examined by again applying a 10 ms change in ϕ_r from 1.0 to 0.6. Heat release rates for both the back-supported and non-back-supported flame are plotted in Figure 5-2. The products side ϕ_b follows the same linear path as ϕ_r, merely shifted forward in time by 2 ms. Back-support strengthens the burning in the flame, and the flames reach appreciably different steady-state heat release rates. Note that the heat release history of the non-back-supported flame equilibrates more slowly because its product side boundary conditions continue to change until $t = 12$ ms, one flame time scale after the change in ϕ_r is complete.

Figure 5-3 uses the same time-dependent calculations but plots the heat release rates in terms of ϕ_r, emphasizing that the effect of back-support is not inherently a dynamic one. Each $\dot{Q}$ is really a function of both ϕ_r and ϕ_b; for the back-supported flame, ϕ_b is always 1.0, while for the non-back-supported flame, ϕ_b lags behind ϕ_r but follows it. Thus the divergence of paths as ϕ_r approaches 0.6: the difference in ϕ_b between the two flames is increasing. The convergence of data points into vertical

[1] U is also updated, indirectly, through Equation 2.30.

groups at $\phi_r = 0.6$ occurs as heat release rates settle from their dynamic values to equilibrium.

Understanding the mechanism of back-support requires an examination of flame structure. Figures 5-4 through 5-7 show temperature and Y_{OH} profiles for the 10 ms change in ϕ_r. Six profiles are shown in each plot, beginning at $t = 0$ and separated by 3 ms intervals. Focusing first on the temperature profiles of the back-supported flame, one can identify high-temperature points at which the slope of the profile sharply decreases; these points generally correspond to the temperature in the reaction zone of the flame. Thus as ϕ_r decreases, the reaction zone temperature decreases, an effect consistent with trends observed in $\dot{Q}$. However, as the reaction zone temperature decreases, the slope on the products side of the reaction zone increases. A diffusive heat flux from the high-temperature, $\phi_b = 1.0$ products stream feeds the reaction zone. In the non-back-supported flame (Figure 5-5), this heat flux is not present. As the reaction zone temperature drops, the products-stream temperature drops accordingly. No high-temperature reservoir of heat is present to strengthen the flame.

The burning of the back-supported flame may also be enhanced by radicals in the products stream, an effect examined with regard to OH in Figures 5-6 and 5-7. The concentration of OH is certainly higher in the reaction zone of the back-supported flame than in the reaction zone of the non-back-supported flame. This could be due to the higher temperature of the back-supported reaction zone, but it may also result, in part, from a change in diffusive fluxes. The concentration of OH in the products stream falls with ϕ_b, and the diffusive flux of OH out of the reaction zone into the products may thus be larger in the non-back-supported flame than in the back-supported flame. This significance of this mechanism is not clear from the given data. Plotting the profile of each term in the OH species conservation equation—reaction and diffusion, in particular—would elucidate the effects of radical back-support.

It is important to note that in all the plots of flame structure (Figures 5-4 through 5-7), the flame tends to shift slightly over time with respect to the computational grid. The location of the reactants-side and products-side boundaries remains fixed in time, however; though initially chosen to closely surround the flame, as described above,

the current formulation does not update the boundary coordinates to account for flame movement. The total range of flame movement does not exceed 0.25 mm, so this inaccuracy is probably quite negligible.

5.2 Unsteady Strain in a Flame-Vortex Interaction

The impact of flow inhomogeneity on burning is studied in the context of the flame-vortex interaction of Figure 1-1. The figure shows four snapshots, separated by 1 ms intervals, of a counterrotating vortex pair moving towards a freely propagating premixed flame. Since the domain is symmetric, only the left half of the interaction is shown. The grayscale indicates temperature and the contour lines indicate vorticity. As discussed in §1.1, the flame surface is stretched and reshaped by the vortex. Data for this figure comes from a direct numerical simulation of two-dimensional reacting flow, performed with detailed chemistry and transport [17, 16].

Now consider the flame element on the centerline of the flame-vortex interaction. As the vortex approaches, strain on the flame element rapidly increases and the burning rate changes as a result. We would like to model the time-dependent burning of this flame element using our elemental flame, thus testing the applicability of the elemental flame as a subgrid model as well as its ability to capture the effects of unsteady strain.

5.2.1 Matching the Leading Edge Strains

The primary input to the elemental flame model must be the strain history of the flame element at the centerline of the two-dimensional simulation. A natural idea is to match the strain at the reactants-side leading edge of the two-dimensional flame with the leading edge strain (ϵ) of the elemental flame. According to the flamelet hypothesis, we should expect the profiles in the elemental flame and the profiles normal to the two-dimensional flame surface to have similar structures; this structural similarity includes profiles of strain (or ϵU, in the elemental flame case). Also, matching of the leading edge strains led to favorable comparison of the elemental flame with

OPPDIF.

The strain tangential to a 99% contour of Y_{CH_4} is thus extracted from the centerline of the flame-vortex interaction. This contour is a reliable indicator of the flame leading edge, so it follows the flame element in a Lagrangian sense. The leading edge strain history is plotted as the solid line in Figure 5-8. This strain and its corresponding Karlovitz number rise 1.6 orders of magnitude over a period comparable to the time scale of the premixed flame. The burning of the flame element clearly will not respond quasi-steadily.

With an input strain history $\epsilon(t)$ in hand, the elemental flame requires only a starting condition and appropriate mixture boundary conditions matching those in the flame-vortex interaction. The premixed flame in the flame-vortex interaction is a stoichiometric methane-air flame with an additional 20% N_2 dilution by volume present in both the reactants and products. This dilution lowers the adiabatic flame temperature from 2230 K to approximately 1900 K, thus reducing the burning rate and lengthening the flame time scale. Dilution is included in the flame-vortex calculation both to reduce the stiffness of the chemistry and to amplify the effects of unsteady strain. Mixture boundary conditions on the elemental flame reflect this dilution but remain fixed in time. Smooke's 46-reaction mechanism (Table 2-1) is used in computing both the flame-vortex interaction and evolution of the elemental flame. The flame-vortex interaction uses a more detailed transport model, identical to that of OPPDIF, but in light of §4.2, the resulting discrepancy should be minimal.

The computed heat release rate of the elemental flame, obtained by matching the leading edge strain histories, is shown by the solid line in Figure 5-9. Circles represent the heat release rate of the two-dimensional flame element, computed by integrating $\dot{w}_T$ along the centerline coordinate of Figure 1-1. Note that the comparison of heat release rates does not extend past $t = 4$ ms; beyond this time, the vortex in the two-dimensional simulation comes within a diameter of the convective boundary conditions at the top of the domain, and the results become numerically questionable. The heat release rate falls with increasing strain in both the one-dimensional (elemental flame) and two-dimensional results—an expected trend—but the elemental

flame clearly underpredicts the heat release rate at the two-dimensional flame surface. This discrepancy widens at higher strains and larger times; the elemental flame even undergoes quenching near $t = 3.5$ ms.

Underprediction of $\dot{Q}$ suggests that the strain in the elemental flame is too high in comparison to that of the two-dimensional flame element. Suspicion of such a strain mismatch is confirmed in Figure 5-10. Here, the solid line represents the strain profile across the centerline element of the two-dimensional flame surface at $t = 2$ ms; the open circle indicates the location and strain of the flame leading edge. The average strain in this flame element, particularly the strain around the reaction zone (indicated by $\dot{w}_T$), is significantly lower than the leading edge strain. Indeed, the strain rate generally seems to fall when moving across the flame from reactants to products, excepting a small hump around the reaction zone. This strain profile differs markedly from that of the elemental flame, as exemplified in Figure 4-3. Strain in the elemental flame rises due to expansion in the reaction zone—from a reactants-side value of ϵ to a products-side value of ϵU_b.

An explanation for the unusual strain profile in the two-dimensional flame element is advanced as follows. Ahead of the flame in Figure 5-10, the strain is observed to decay quite rapidly. This strain profile comes only from the vortex (which sits to the left of the figure boundary), not from the flame. Extrapolating this non-reacting strain into the flame region, the dashed line continues to represent the strain profile in the absence of reaction, due only to decay around the vortex. The vortex-induced non-reacting strain is in a sense the *underlying strain* in the flame region. Expansion within the flame *adds* to the underlying strain to produce the measured strain profile (the solid line), but the underlying decay in strain insures that the measured strain falls towards the products side.

This flame-vortex interaction may thus be on the boundary of the flamelet regime. The strain imposed by the vortex on the flame is varying over the length scale of the flame, while an essential flamelet assumption is that the flame should be thin with respect to length scales in the flow. In the elemental flame, developed under these flamelet assumptions, the underlying strain is constant and equal to ϵ, for in the

absence of reaction, the velocity field would collapse to that of a pure stagnation point flow.

5.2.2 Matching Average Strains

Though the flame-vortex interaction of Figure 1-1 may not be an ideal test case for the flamelet concept, it still represents a flow regime of practical importance. A correction is thus proposed to extend the accuracy of our subgrid model. Rather than matching strains at the leading edges, the *average strain* in the two-dimensional flame element should be matched to the average strain in the elemental flame.

The average strain in the elemental flame, $\bar{\epsilon}_{1d}$, is defined arithmetically

$$\bar{\epsilon}_{1d} = \epsilon \left(\frac{1 + U_b}{2} \right) \tag{5.1}$$

where ϵ is the usual reactants-side strain. (Use of the geometric mean was also investigated, but found to give less accurate results.) Two methods are proposed for extracting the two-dimensional average strain, $\bar{\epsilon}_{2d}$. The first method supposes the average strain to equal the strain at the heat release peak. Because the 10% contour of Y_{CH_4} has been found to follow the heat release peak fairly closely [17], the strain tangent to the 10% contour of Y_{CH_4} is extracted from the centerline and deemed the 'center' average. The second method for extracting $\bar{\epsilon}_{2d}$ takes the arithmetic mean of two strains at each timestep: the leading edge strain, again calculated at the 99% contour of Y_{CH_4}, and the trailing edge strain, calculated at the 90% contour of Y_{CO_2}. This mean value is deemed the 'two-point' average strain. Both of the resulting strain histories $\bar{\epsilon}_{2d}(t)$ are shown in Figure 5-8. To confirm that the 10% contour of Y_{CH_4} does indeed follow the reaction zone center, the figure plots $\times$ marks periodically, denote the strain directly measured at the $\dot{w}_T$ maximum. The 10% criterion matches well with these marks, slightly overestimating the center strain only for $t > 3$ ms.

The elemental flame requires the reactants-side strain ϵ as an input to each time step. The inversion of Equation 5.1 to calculate ϵ from $\bar{\epsilon}_{1d} = \bar{\epsilon}_{2d}$ is not as straightforward as it may seem, however. For unsteady strains, U_b is a function of ϵ and $\frac{1}{\epsilon}\frac{\partial \epsilon}{\partial t}$,

according to the instantaneous solution of the ODE in Equation 2.30. Consequently, Equations 5.1 and 2.30 must be combined to yield a single ODE, which is then integrated implicitly to find U_b from $\bar{\epsilon}_{1d}(t)$. The solution for U_b is substituted back into Equation 5.1 to yield ϵ.

Outputs from the elemental flame code obtained by matching the average strain histories are shown in Figure 5-9. The dashed line, corresponding to the center average, tends to overpredict the heat release rate at initial times, implying that the heat release peak may under-represent the optimal strain. The dash-dotted line, corresponding to the two-point average, shows closer agreement with the actual two-dimensional heat release rate, diverging only at high strains and large time. In general, both methods of defining the average strain on the two-dimensional flame surface and matching it to the average strain on the elemental flame show a marked improvement over the matching of leading edge strains explored in the previous section.

To illustrate the unsteady response of burning to these rapid changes in strain, steady-state reference points are included in Figure 5-9. These points, computed with the elemental flame, are the steady-state values of the heat release rate at average strains corresponding to the instantaneous two-point averages extracted from the two-dimensional simulation. For $t \geq 3.5$ ms, burning persists under the dynamically applied strain, though at steady-state the flame would have undergone quenching. With the average strain as an input, the elemental flame model captures this important unsteady effect.

Figure 5-11 compares the instantaneous structure of the elemental flame using the two-point average with the structure of the two-dimensional flame; both sets of profiles are taken at $t = 2$ ms, where the heat release rates match closely. This comparison highlights the inherent difficulty of making the elemental flame exactly predict the two-dimensional burning. Though the average strains in the two flame regions are equal, the strain distributions are profoundly different. Disagreement in the strain distributions causes the remaining scalar profiles to differ in shape, as demonstrated here by the temperature. These differences in shape in turn affect the diffusive fluxes, which feed into the complex mechanics of the reaction zone.

It is notable that the strain at center of the reaction zone, i.e. at the peak of $\dot{w}_T$, did not provide the best characterization of the two-dimensional burning. This result is tempered by the fact that strain at the *true* reaction zone center falls below our continuous strain history at later times. Still, examining all the computed burning rate histories in light of the two-dimensional flame structure suggests a path to more accurate application of the elemental flame: as strain on the premixed flame increases, the reaction zone moves further into the products side, where in the two-dimensional flame, the strain is lower. Overprediction of the strain at $t > 3$ ms may really be a symptom of overpredicting the strain at higher strains. A weighted average of strain over the reaction zone, always following the reaction zone in time, may thus provide the best characterization of two-dimensional burning. Weighing the strain over the entire reaction zone rather than just at its peak should better capture the diffusive fluxes feeding chemical reaction and perhaps avoid overestimating the burning at low strains.

Finally, an important addition to this analysis would involve applying the elemental flame subgrid model to a flame surface strained by a weaker vortex—a vortex for which the length scale of the underlying strain rate variation is large. Equivalently, one could examine slices of the current two-dimensional flame surface farther from the vortex than the centerline flame element examined here.

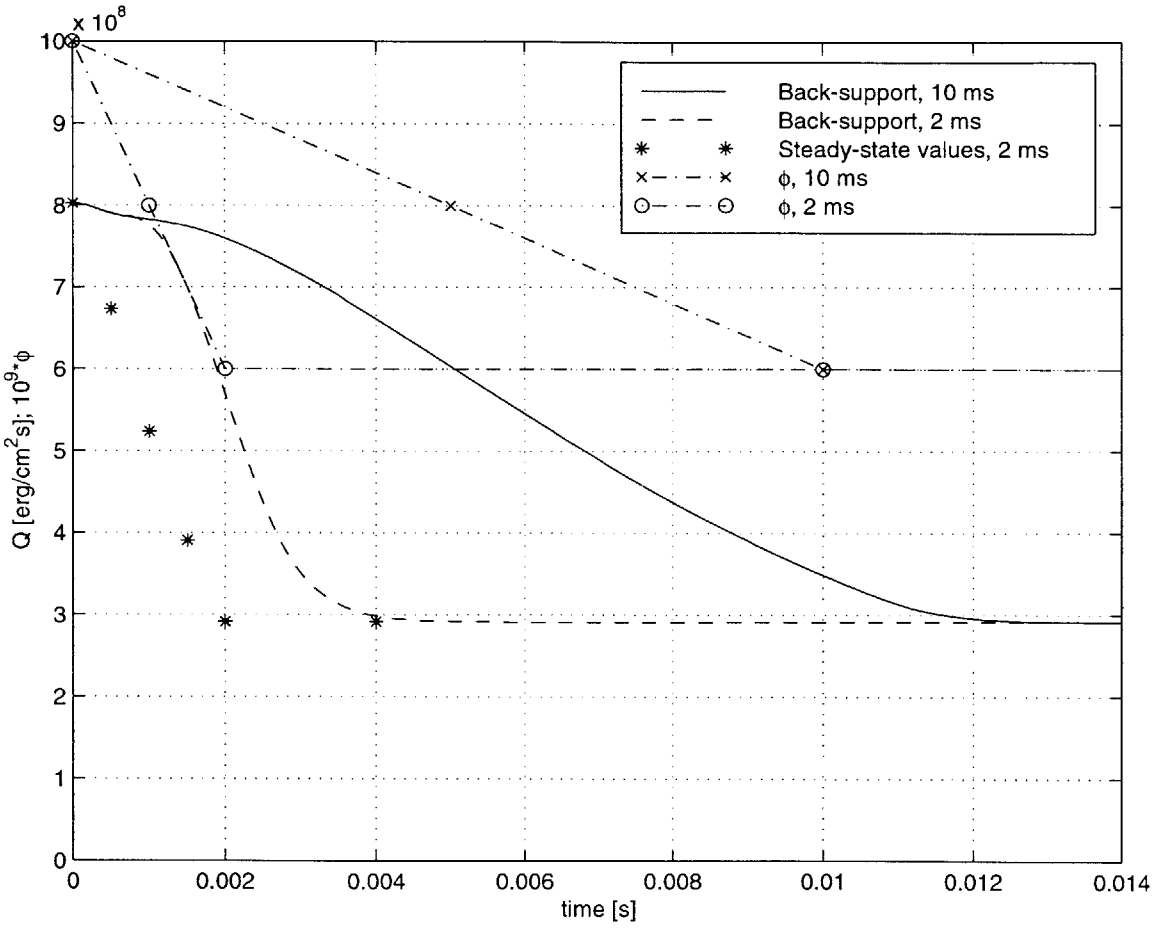

Figure 5-1: Heat release rate vs. time for linear changes in ϕ; $\epsilon = 300$.

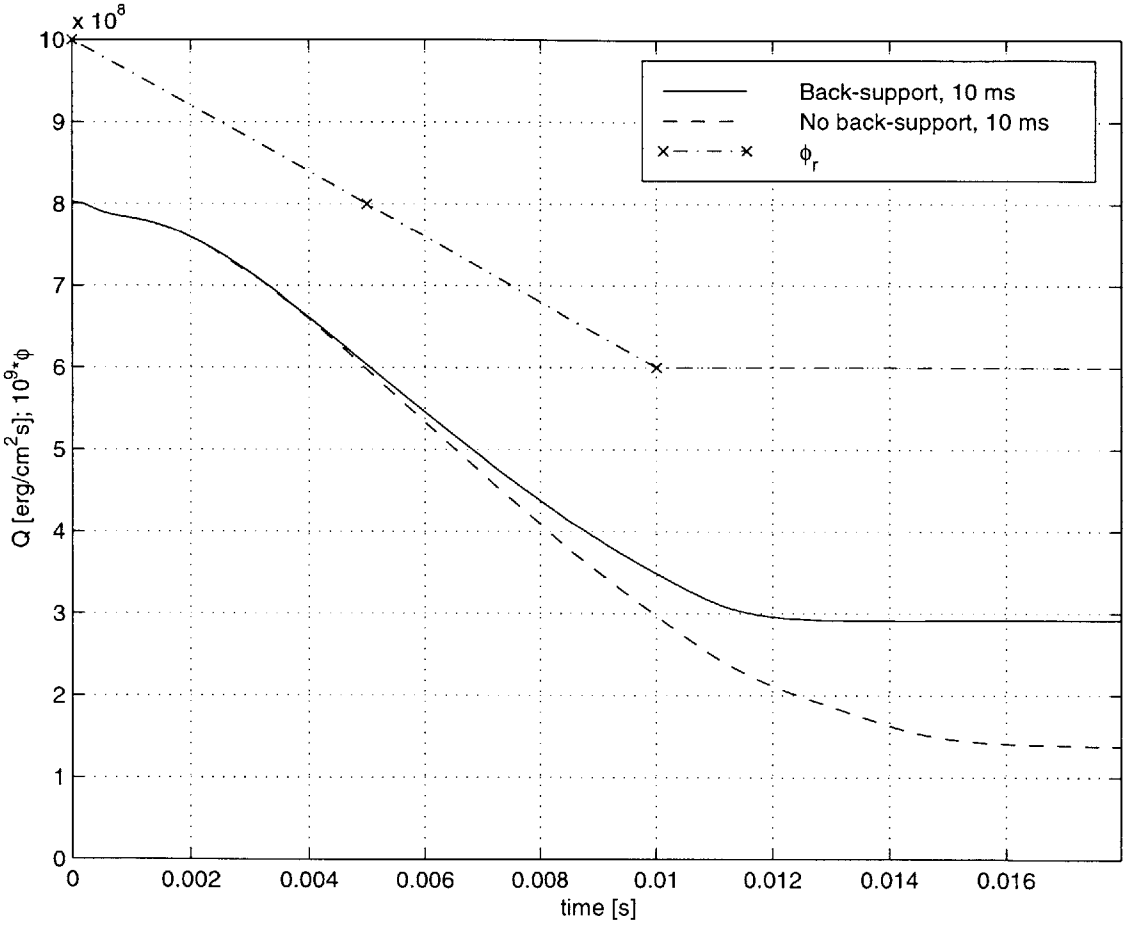

Figure 5-2: Heat release rate vs. time, back-support and no back-support.

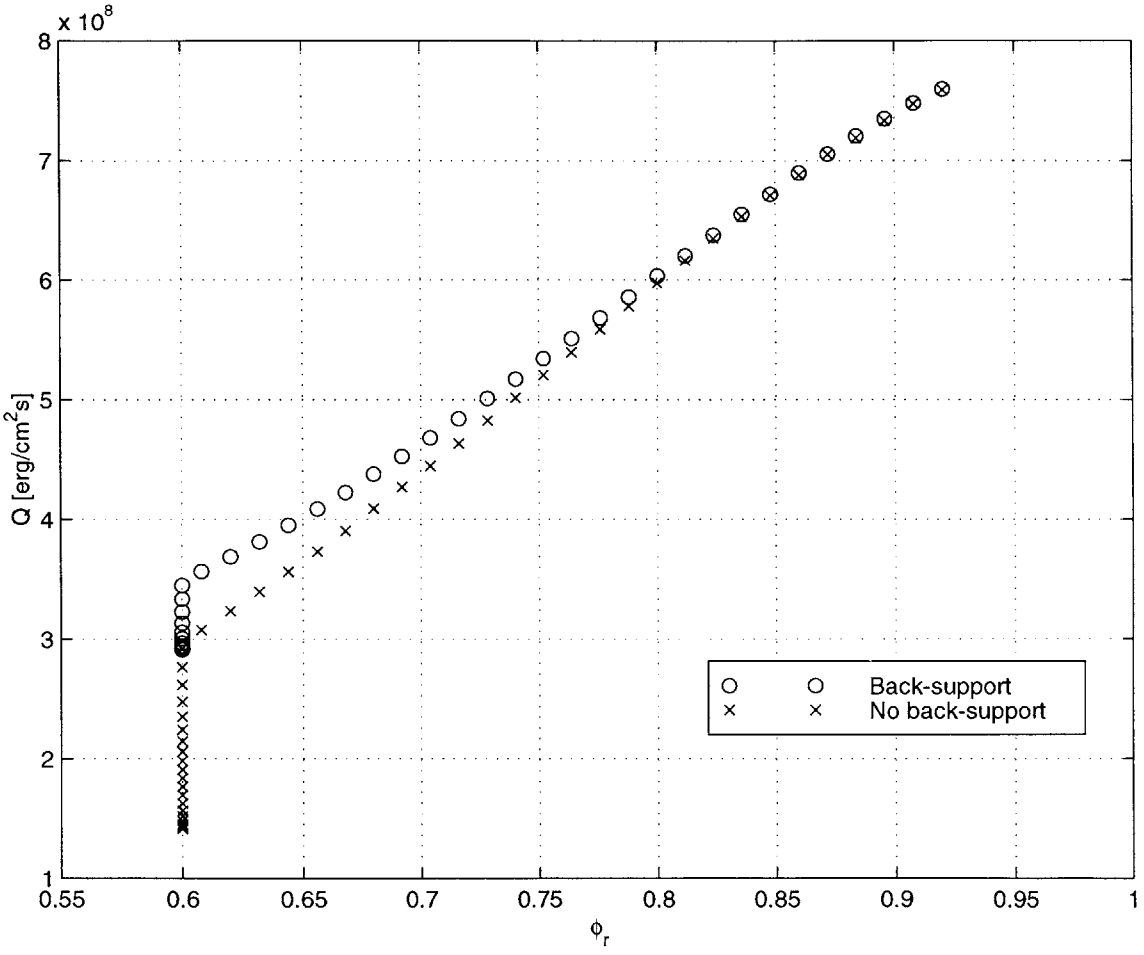

Figure 5-3: Heat release rate vs. reactants equivalence ratio, back-support and no back-support.

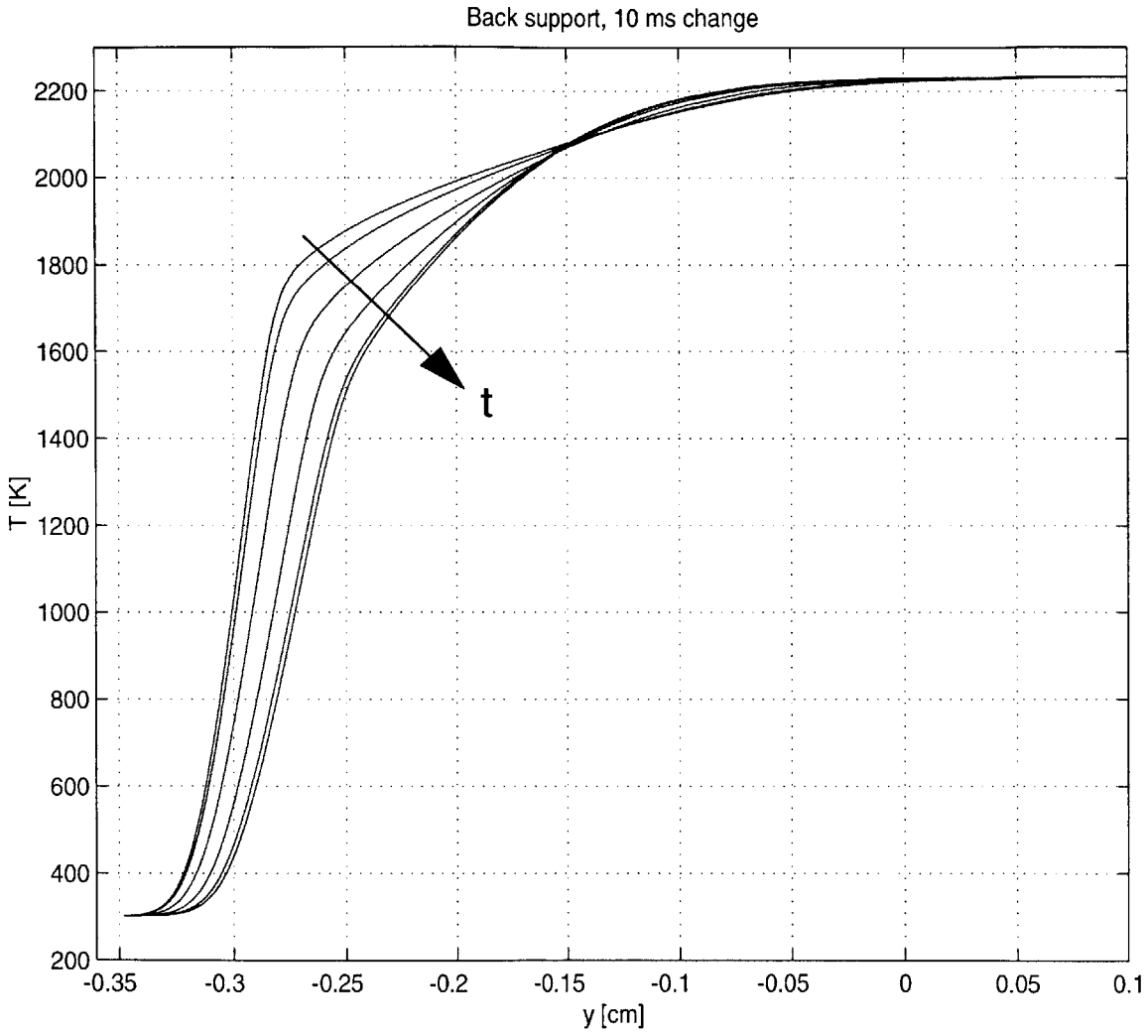

Figure 5-4: Temperature profiles with changing ϕ, back-supported flame; $\Delta t = 3$ ms.

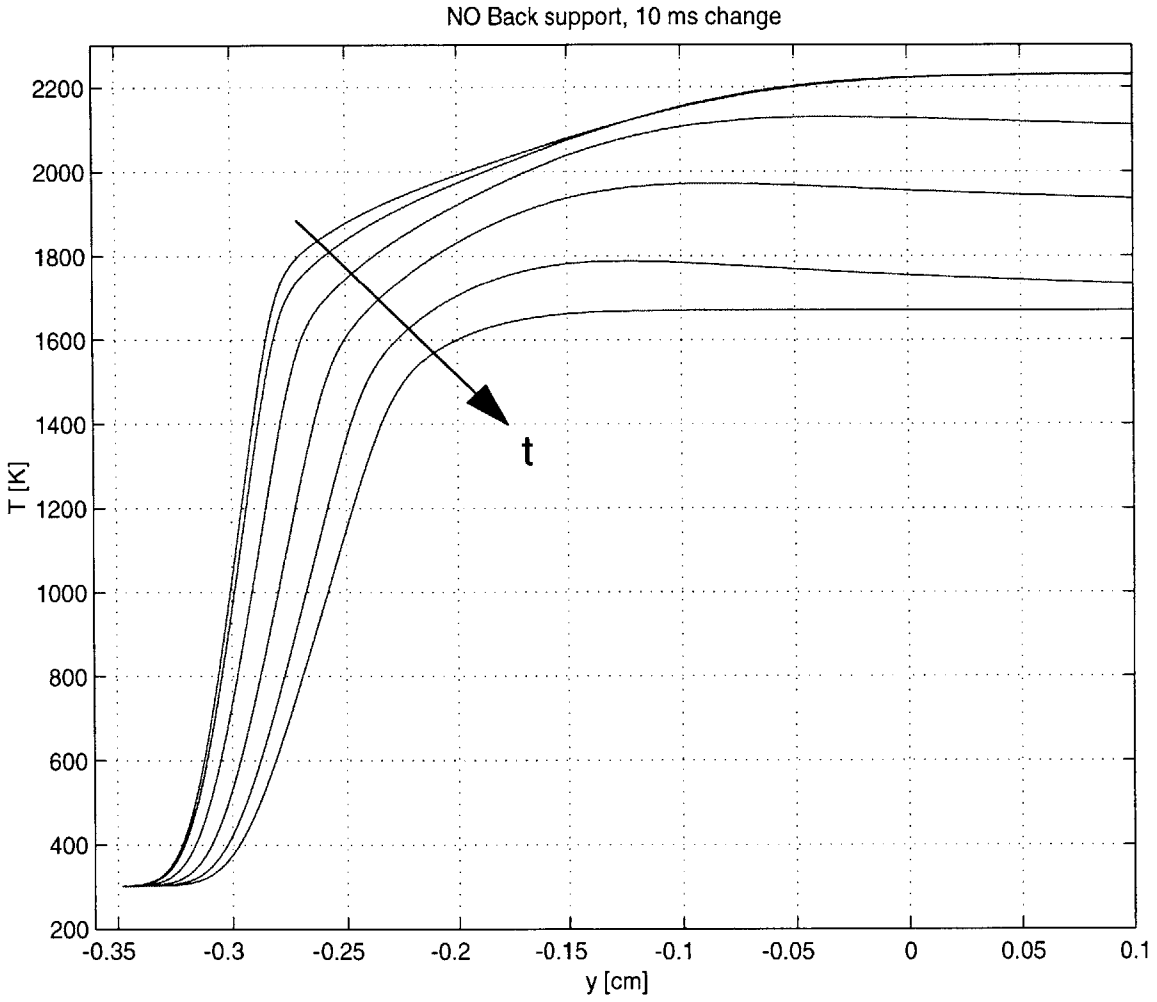

Figure 5-5: Temperature profiles with changing ϕ, non-back-supported flame; $\Delta t = 3$ ms.

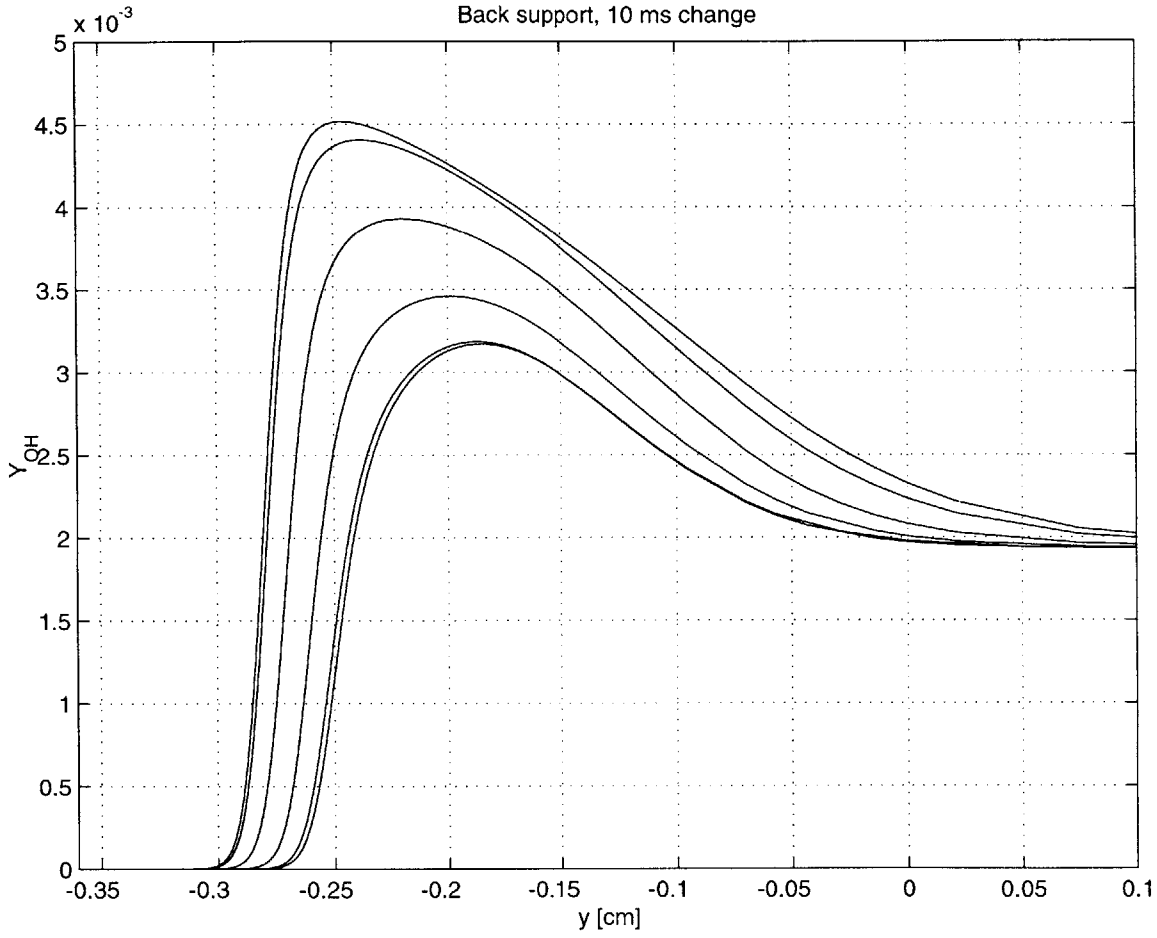

Figure 5-6: OH profiles with changing ϕ, back-supported flame; $\Delta t = 3$ ms.

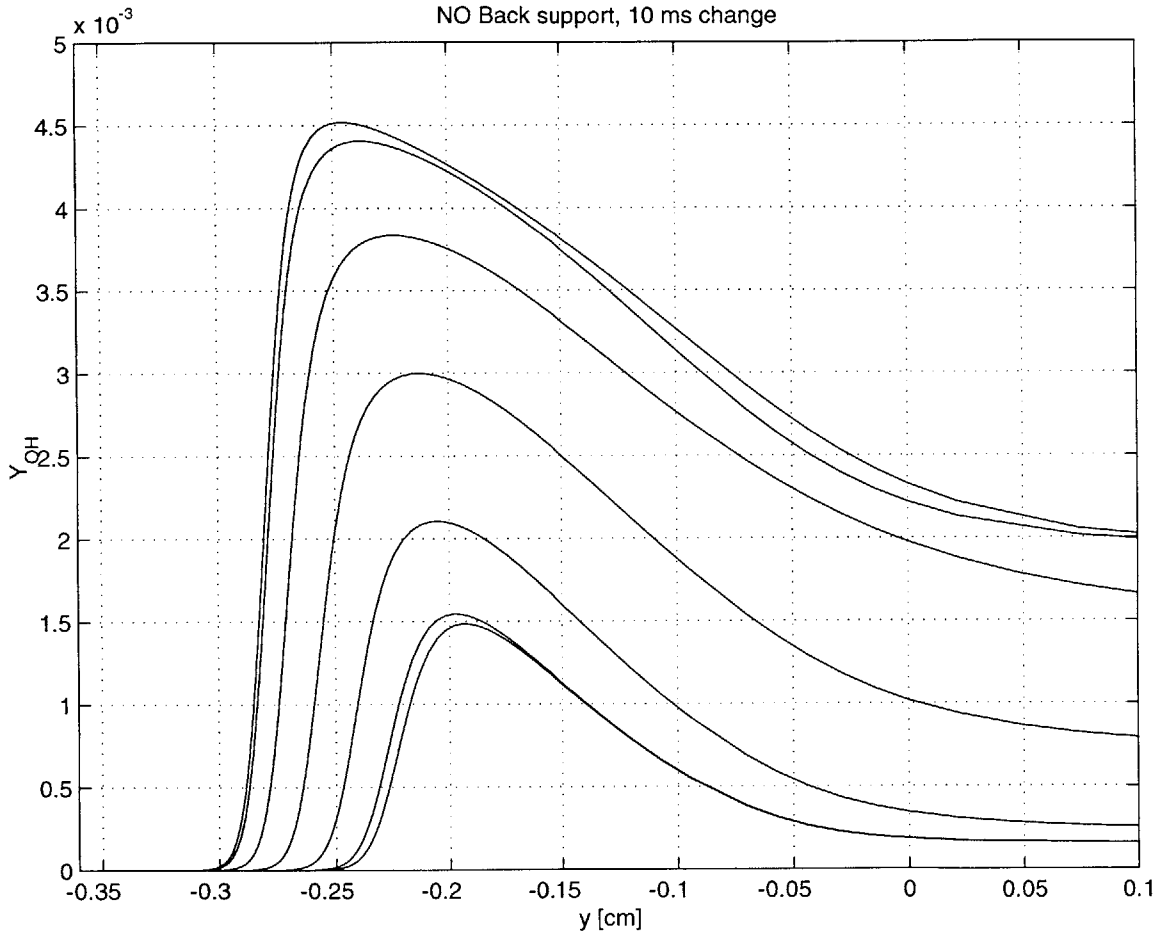

Figure 5-7: OH profiles with changing ϕ, non-back-supported flame; $\Delta t = 3$ ms.

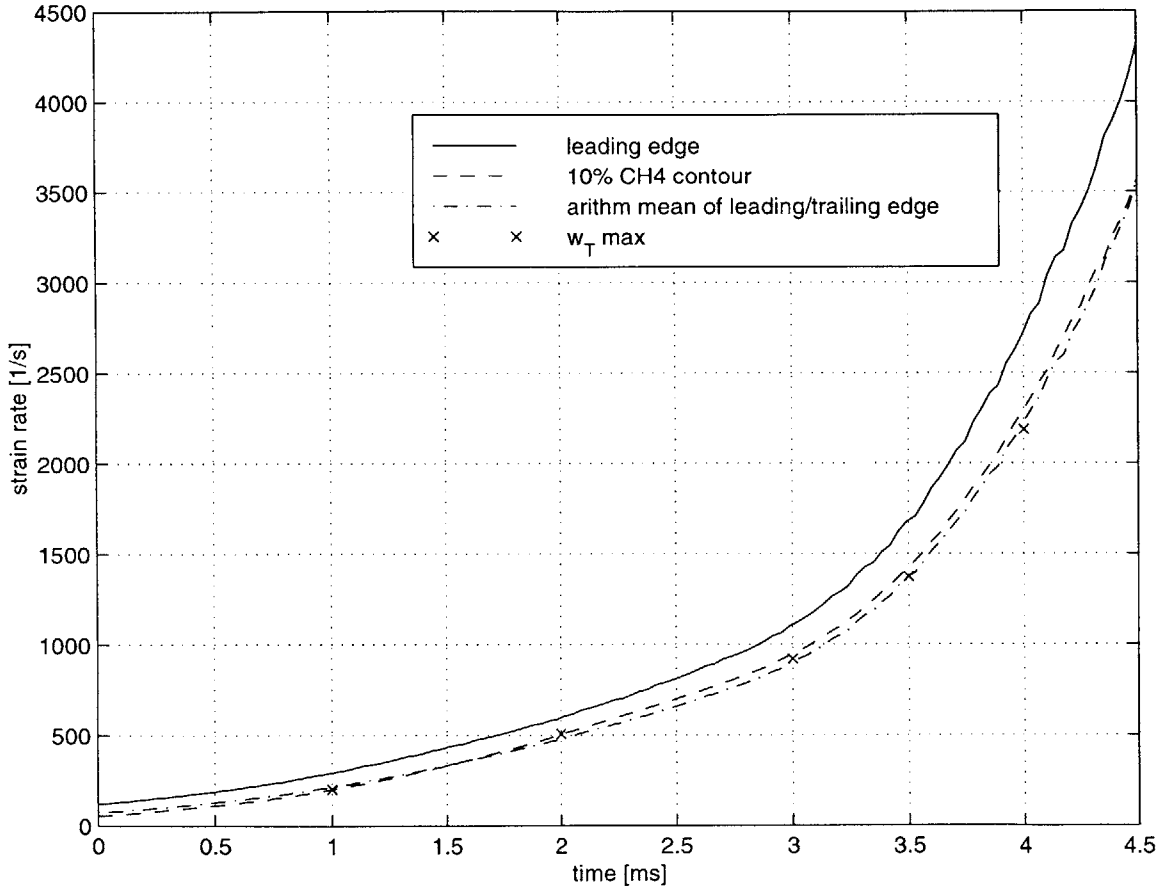

Figure 5-8: Strain histories extracted from the flame-vortex interaction.

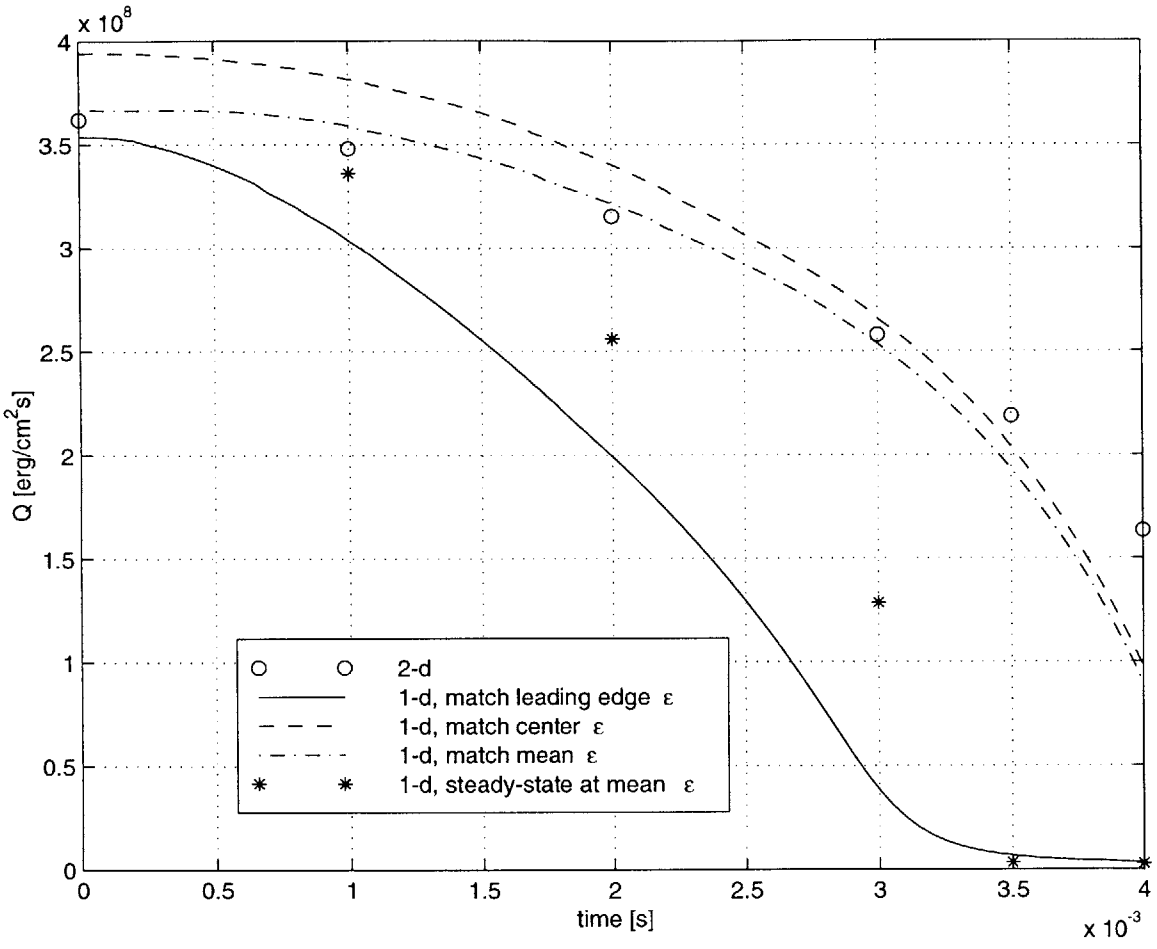

Figure 5-9: One- and two-dimensional heat release rates vs. time for various strain-matching schemes.

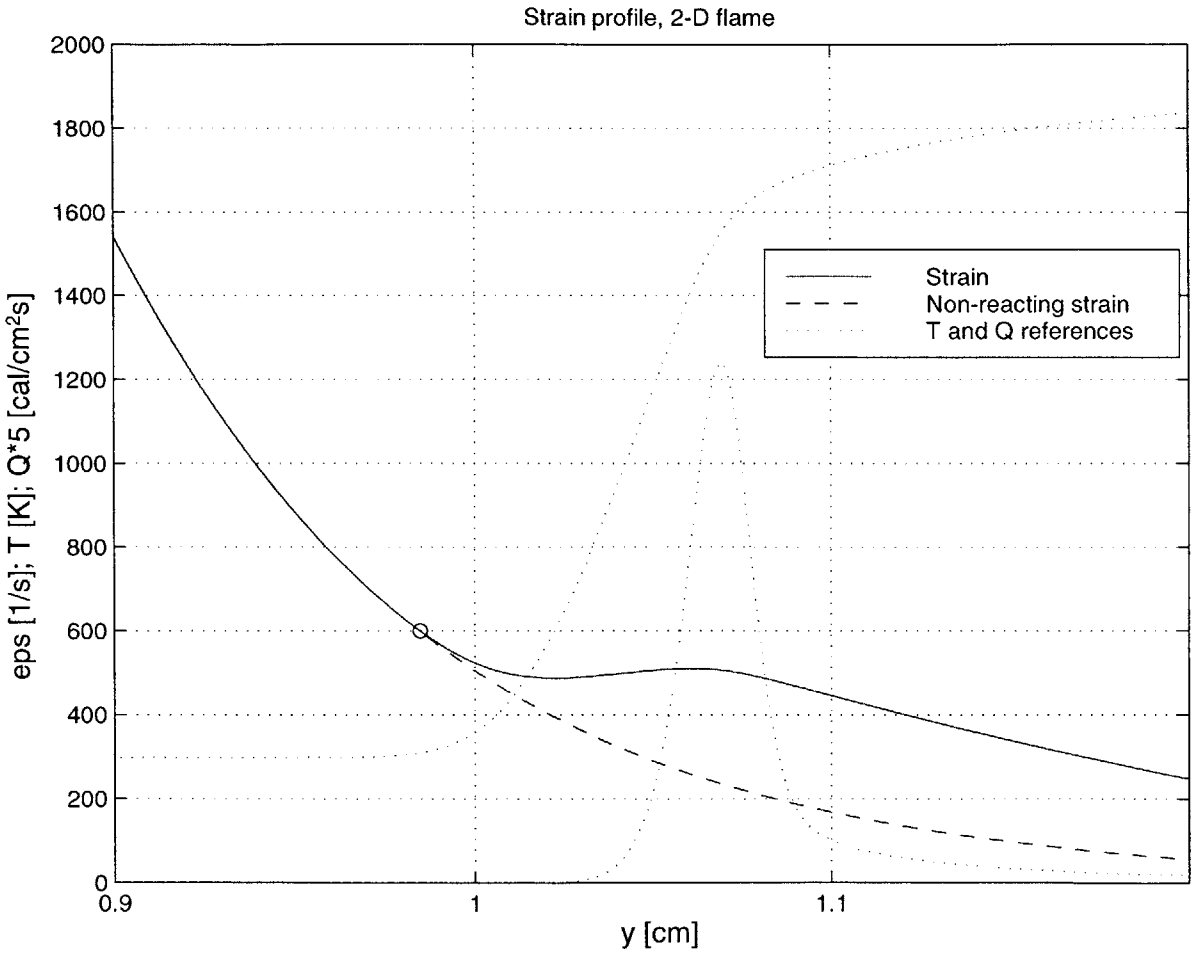

Figure 5-10: Strain profile in the two-dimensional flame element; $t = 2$ ms.

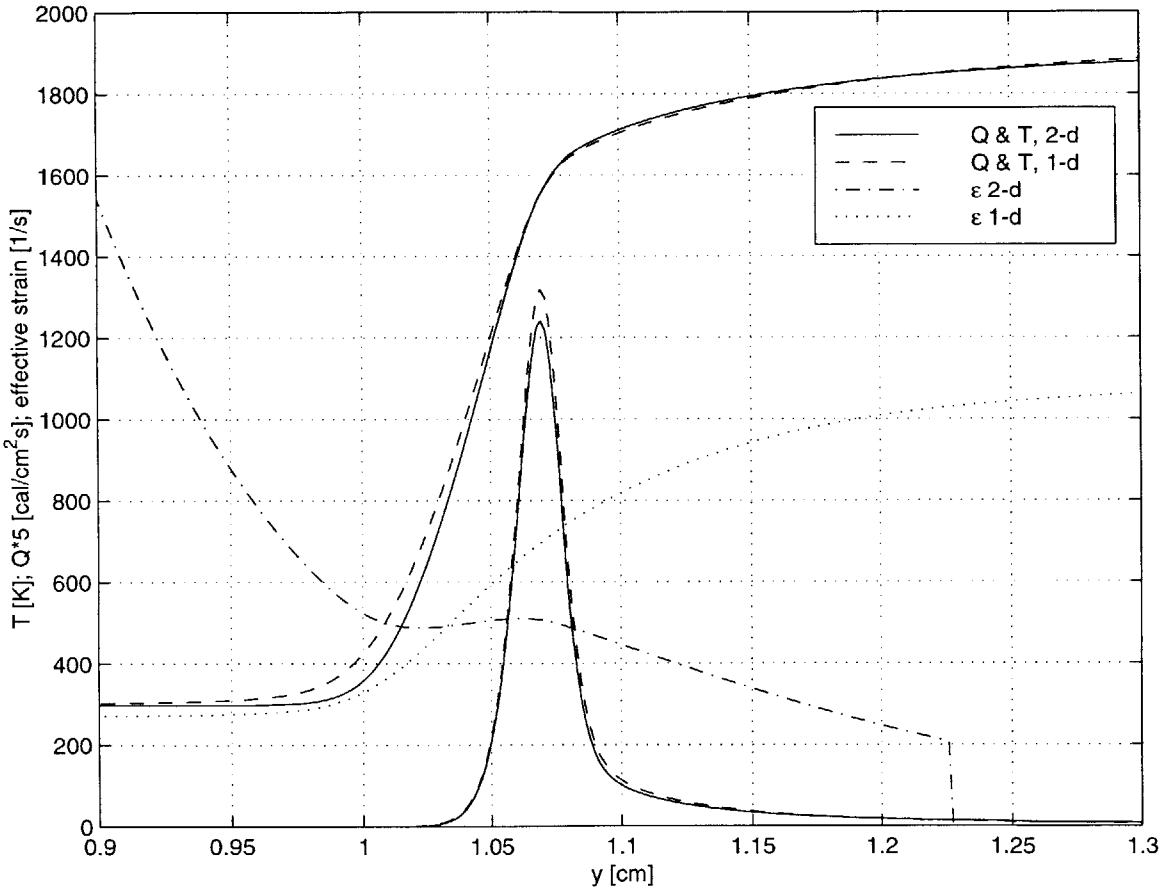

Figure 5-11: Structure of the one- and two-dimensional flame elements; $t = 2$ ms.

Chapter 6

Conclusions and Further Work

The preceding chapters have developed a robust and efficient computational model for combustion under arbitrarily varying strain rate and mixture composition. In its most basic form, the elemental flame model provides a rich data set for analyzing kinetic and transport processes within flames. Reduction of this data set can yield fundamental insights into the mechanisms of unsteady flame response, by linking detailed flame structure to the modeling of flame dynamics.

The unsteady interactions described at the outset of this research were examined in carefully-defined but practical contexts. Equivalence-ratio variation on the order of a flame time scale produced a dynamic burning response and modified the flame structure. It remains to develop a more elegant method of updating the composition of the products stream of the non-back-supported flame, one that reformulates the role of the products stream in the context of a Lagrangian transformation. The unsteady strain applied by a vortex to a two-dimensional flame surface allowed burning to persist at strains far higher than the steady-state values at quenching. Use of the elemental flame as a subgrid model in this context concluded with an important refinement to the flame embedding and flamelet approaches: the key parameter governing burning at a premixed flame surface is the average strain, not the cold strain at the reactants-side leading edge. Further development must clarify how to best define this average.

The simplicity of the elemental flame model makes possible numerous extensions,

with wide applicability. Radiation or some other heat loss term can be included to more realistically model flame extinction. Adding the appropriate chemical kinetics could lead to accurate NO_x predictions, based on the detailed flame structure. The unsteady evolution of the elemental flame could be used to simulate control feedback and actuation; instantaneously computed burning parameters of the elemental flame could be used within an arbitrary control law. Additionally, the detailed computation of the elemental flame can be used to develop and validate lower-order models for the control of flame dynamics.

Bibliography

[1] A. M. Bruaset, A. Tveito, and R. Winther. On the stability of relaxed incomplete LU factorizations. *Mathematics of Computation*, 54:701–719, 1990.

[2] R. S. Cant, K. N. C. Bray, L. W. Kostiuk, and B. Rogg. Flow divergence effects in strained laminar flamelets for premixed turbulent combustion. *Combustion Science and Technology*, 95:261–276, 1994.

[3] N. Darabiha. Transient behaviour of laminar counterflow hydrogen-air diffusion flames with complex chemistry. *Combustion Science and Technology*, 86:163–181, 1992.

[4] Tarek Echekki and Jacqueline H. Chen. Unsteady strain rate and curvature effects in turbulent premixed methane-air flames. *Combustion and Flame*, 106:184–202, 1996.

[5] Fokion N. Egolfopoulos. Dynamics and structure of unsteady, strained, laminar premixed flames. In *25th Symposium (International) on Combustion*, pages 1365–1373. The Combustion Institute, 1994.

[6] Fokion N. Egolfopoulos and Charles S. Campbell. Unsteady counterflowing strained diffusion flames: diffusion-limited frequency response. *Journal of Fluid Mechanics*, 318:1–29, 1996.

[7] Stanley C. Eisenstat and Homer F. Walker. Globally convergent inexact Newton methods. *SIAM Journal on Optimization*, 4:393–422, 1994.

[8] Howard C. Elman. A stability analysis of incomplete LU factorizations. *Mathematics of Computation*, 47:191–217, 1986.

[9] Ahmed F. Ghoniem, Marios C. Soteriou, Omar M. Knio, and Baki Cetegen. Effect of steady and periodic strain on unsteady flamelet combustion. In *24th Symposium (International) on Combustion*, pages 223–230. The Combustion Institute, 1992.

[10] Gene H. Golub and Charles F. van Loan. *Matrix Computations*. The Johns Hopkins University Press, Baltimore, third edition, 1996.

[11] H. G. Im, J. K. Bechtold, and C. K. Law. Counterflow diffusion flames with unsteady strain rates. *Combustion Science and Technology*, 106:345–361, 1995.

[12] Robert J. Kee, James A. Miller, Gregory H. Evans, and Graham Dixon-Lewis. A computational model of the structure and extinction of strained opposed-flow premixed methane-air flames. In *22nd Symposium (International) on Combustion*, pages 1479–1494. The Combustion Institute, 1988.

[13] J. S. Kistler, C. J. Sung, T. G. Kreutz, C. K. Law, and M. Nishioka. Extinction of counterflow diffusion flames under velocity oscillations. In *26th Symposium (International) on Combustion*, pages 113–120. The Combustion Institute, 1996.

[14] Randall J. LeVeque. *Numerical Methods for Conservation Laws*. Birkhauser Verlag, Basel, second edition, 1992.

[15] A. E. Lutz, R. J. Kee, J. F. Grcar, and F. M. Rupley. OPPDIF: A Fortran program for computing opposed-flow diffusion flames. Technical Report SAND96-8243, Sandia National Laboratories, May 1997.

[16] H. N. Najm, R. W. Schefer, R. B. Milne, C. J. Mueller, K. D. Devine, and S. N. Kempka. Numerical and experimental investigation of vortical flow-flame interaction. Technical Report SAND98-8232, Sandia National Laboratories, February 1998.

[17] Habib N. Najm, Phillip H. Paul, Charles J. Mueller, and Peter S. Wyckoff. On the adequacy of certain experimental observables as measurements of the flame burning rate. *Combustion and Flame*, 113:312–332, 1998.

[18] Habib N. Najm, Peter S. Wyckoff, and Omar M. Knio. A semi-implicit numerical scheme for reacting flow; stiff chemistry. *Journal of Computational Physics*, 143:381–402, 1998.

[19] Michael Pernice and Homer F. Walker. NITSOL: A Newton iterative solver for nonlinear systems. *SIAM Journal on Scientific Computing*, 19:302–318, 1998.

[20] N. Peters and R. J. Kee. The computation of stretched laminar methane-air diffusion flames using a reduced four-step mechanism. *Combustion and Flame*, 68:17–29, 1987.

[21] Norbert Peters. Length scales in laminar and turbulent flames. In Elaine S. Oran and Jay P. Boris, editors, *Numerical Approaches to Combustion Modeling*, chapter 6, pages 155–182. AIAA, Washington, DC, 1991.

[22] Constantin Petrov. *Numerical Simulation of Reacting Flows with Complex Chemistry Using Flame Embedding.* Ph.D. thesis, Massachusetts Institute of Technology, Department of Mechanical Engineering, February 1997.

[23] Constantin Petrov and Ahmed Ghoniem. An unsteady strained flame model for turbulent combustion simulations. In *32nd Aerospace Sciences Meeting and Exhibit*, number AIAA-94-0776. AIAA, January 1994.

[24] Constantin Petrov and Ahmed Ghoniem. The transient response of strained laminar-premixed flames. *Combustion and Flame*, 102:401–417, 1995.

[25] Constantin Petrov and Ahmed Ghoniem. An unsteady strained flame model with multi-step chemical kinetics for turbulent combustion simulations. In *33rd Aerospace Sciences Meeting and Exhibit*, number AIAA-95-0380. AIAA, January 1995.

[26] Constantin Petrov and Ahmed Ghoniem. A uniform strain model of elemental flames in turbulent combustion simulations. *Combustion and Flame*, 111:47–64, 1997.

[27] T. Poinsot, D. Veynante, and S. Candel. Diagrams of premixed turbulent combustion based on direct simulation. In *23rd Symposium (International) on Combustion*. The Combustion Institute, 1990.

[28] Alberto Pueyo and David W. Zingg. Efficient Newton-Krylov solver for aerodynamic computations. *AIAA Journal*, 36:1991–1997, 1998.

[29] G. A. Richards, M. C. Janus, and E. H. Robey. Control of flame oscillations with equivalence ratio modulation. *Journal of Propulsion and Power*, 15(2):232–240, 1999.

[30] Yousef Saad. *Iterative Methods for Sparse Linear Systems*. PWS Publishing, Boston, 1996.

[31] K. Sardi, A. M. K. P. Taylor, and J. H. Whitelaw. Mixing model for the calculation of extinction in oscillating flames. *AIAA Journal*, 37(6):751–758, 1999.

[32] John Shadid, Raymond S. Tuminaro, and Homer F. Walker. An inexact Newton method for fully-coupled solution of the navier-stokes equations with heat and mass transport. Technical Report SAND97-0132, Sandia National Laboratories, February 1997.

[33] Mitchell D. Smooke, editor. *Reduced Kinetic Mechanisms and Asymptotic Approximations for Methane-Air Flames*. Lecture Notes in Physics. Springer-Verlag, Berlin, 1990.

[34] G. Stahl and J. Warnatz. Numerical investigation of time-dependent properties and extinction of strained methane- and propane-air flamelets. *Combustion and Flame*, 85:285–299, 1991.

[35] C. J. Sung, J. B. Liu, and C. K. Law. Structural response of counterflow diffusion flames to strain rate variations. *Combustion and Flame*, 102:481–492, 1995.

[36] Lloyd N. Trefethen and David Bau. *Numerical Linear Algebra.* SIAM, Philadelphia, 1997.

[37] Forman A. Williams. *Combustion Theory.* Addison-Wesley, Reading, MA, second edition, 1985.

[38] A. O. zur Loye and F. V. Bracco. Two-dimensional visualization of premixed-charge flame structure in an IC engine. Technical Report 870454, Society of Automotive Engineers, February 1987.